Geochemistry, Geophysics, Geosystems®

RESEARCH ARTICLE
10.1029/2023GC011389

Lawsonite and Garnet Oxygen Isotope Record of Fluid-Rock Interaction During Subduction

Patricia Kang[1,2], Laure A. J. Martin[3], Alberto Vitale Brovarone[4,5,6], and Donna L. Whitney[1]

[1]Department of Earth & Environmental Sciences, University of Minnesota, Minneapolis, MN, USA, [2]Department of Earth Sciences, University of Arizona, Tucson, AZ, USA, [3]Centre for Microscopy, Characterisation and Analysis, The University of Western Australia, Perth, WA, Australia, [4]Department of Biological, Geological, and Environmental Sciences, University of Bologna, Bologna, Italy, [5]Institut de Minéralogie, de Physique des Matériaux et de Cosmochimie (IMPMC), Sorbonne Université, Muséum National d'Histoire Naturelle, UMR CNRS 7590, IRD UR206, Paris, France, [6]Institute of Geosciences and Earth Resources, National Research Council of Italy, Pisa, Italy

Abstract During the subduction of an oceanic plate, fluids are released from metabasaltic crust, metasediment, and serpentinite under high-pressure/low-temperature conditions. Although some fluids may eventually leave the slab, some participate in metamorphic reactions within the slab during subduction and exhumation. To identify fluid sources and other controls influencing mineral composition, we report the in situ-measured $\delta^{18}O$ of lawsonite and garnet in blueschist- to eclogite-facies rocks from 10 subduction zones that represent various field settings, including mélanges, structurally coherent terranes, and an eclogite xenolith derived from a subducted plate. Lawsonite records distinct $\delta^{18}O$ depending on the host rock type and other rock types that were fluid sources during lawsonite growth. In general, lawsonite in metabasalt (7.6 ± 0.2–14.8 ± 1.1‰) is isotopically lighter than in metasediment (20.6 ± 1.4–24.1 ± 1.3‰) but heavier than in metagabbro (4.0 ± 0.4–7.9 ± 0.3‰). The extent of $\delta^{18}O$ fractionation was evaluated for lawsonite–fluid and lawsonite–garnet pairs as a function of temperature (T). Results demonstrate that variations of >1.7‰ in lawsonite and >0.9‰ in garnet are not related to changing T. More likely, the relative contributions of fluids derived from isotopically heavier lithologies (e.g., sediments) versus lighter lithologies (e.g., ultramafic rocks) are the major control. Monte Carlo simulations were performed to investigate the sources of metasomatic fluids and the water/rock ratio that formed lawsonite-bearing metasomatite. Results indicate that $\delta^{18}O_{Lws}$ and $\delta^{18}O_{Grt}$ record interactions with fluids sourced from diverse lithologies (sediment, serpentinite), further supporting that $\delta^{18}O_{Lws}$ is a useful indicator of subduction fluid-rock interactions.

Plain Language Summary Lawsonite and garnet are silicate minerals that occur in a wide range of rock types (e.g., metamorphosed oceanic crust, sediment) in oceanic subduction zones. They remain stable at great depths under high-pressure/low-temperature (HP/LT) conditions. Consequently, the composition of lawsonite and garnet can serve as a useful recorder of fluid-rock interactions that likely took place under HP/LT conditions during the subduction and exhumation of the oceanic plate. This study presents a comprehensive data set of oxygen isotope analyses for lawsonite and garnet in HP/LT rocks from 10 oceanic subduction zones. The results indicate that lawsonite oxygen isotope composition is largely influenced by the host rock type. In general, lawsonite in metasediments is isotopically heavier than that in oceanic crustal (metamafic) rocks. Despite occurring in a similar type of host rock, significant variations in oxygen isotope composition were observed within individual lawsonite and garnet grains as well as among different samples and subduction zones. These variations are likely attributed to the variable contributions of fluids sourced from isotopically distinct rock types. If the fluids had substantially different isotopic compositions and/or infiltrated at high water/rock (≥1), fluid-rock interactions could have significantly modified the original oxygen isotope composition of host rocks.

Key Points:

- The oxygen isotope composition of lawsonite is strongly influenced by the host rock protolith
- Interactions with fluids and/or isotopic fractionation with coexisting minerals also influence lawsonite and garnet $\delta^{18}O$
- $\delta^{18}O$ in both lawsonite and garnet is a useful indicator of fluid sources and fluid-rock interactions in oceanic subduction zones

Supporting Information:

Supporting Information may be found in the online version of this article.

Correspondence to:

P. Kang,
pkang@arizona.edu

Citation:

Kang, P., Martin, L. A. J., Vitale Brovarone, A., & Whitney, D. L. (2024). Lawsonite and garnet oxygen isotope record of fluid-rock interaction during subduction. *Geochemistry, Geophysics, Geosystems*, *25*, e2023GC011389. https://doi.org/10.1029/2023GC011389

Received 15 DEC 2023
Accepted 25 MAR 2024

1. Introduction

Fluids in subduction zones are important because of their role in transferring elements between different lithologies (Elliott, 2004; You et al., 1996) and dictating the location and extent of flux-melting in the mantle (Grove et al., 2006; Kelley et al., 2010). In situ-measured oxygen isotope analysis of garnet in exhumed high-pressure/low-temperature (HP/LT) rocks is a widely used tool to investigate evidence of fluid-rock interactions in subduction zones (Bovay et al., 2021; Cruz-Uribe et al., 2021; Errico et al., 2013; Martin, Rubatto, et al., 2014;

Page et al., 2014). Garnet is a nominally anhydrous mineral that is commonly found in HP/LT rocks and its oxygen isotope composition is not very susceptible to intracrystalline diffusion (Coghlan, 1990; Page et al., 2010; Scicchitano et al., 2022). These characteristics allow garnet to retain important records of fluid-rock interactions in the form of zoning.

Lawsonite is a hydrous silicate mineral ($CaAl_2Si_2O_7(OH)_2H_2O$) that occurs across a wide range of bulk-rock compositions (e.g., metabasalt, calc-silicate, quartzite) at HP/LT conditions up to ∼300 km in subduction zones (Forneris & Holloway, 2003; Schmidt & Poli, 1998). Because lawsonite is a major host of H_2O (∼11.5 wt %) and trace elements (e.g., Sr, Pb, U, Th, REE) (Fornash et al., 2019; Martin, Hermann, et al., 2014; Whitney et al., 2020), its composition and zoning can record interactions with fluids sourced from chemically distinct lithologies (e.g., serpentinized mantle, altered oceanic crust, sediment) during its growth (Fornash & Whitney, 2020; Kang et al., 2022; Whitney et al., 2020). However, the oxygen isotope composition of lawsonite and its partitioning during fluid-rock interactions at subduction zones have not been systematically investigated due in part to the limited understanding of the potential matrix effect arising from compositional variability of lawsonite (Melnik et al., 2023) and the effects of temperature (Taylor & Coleman, 1968; Vho et al., 2019) and intracrystalline diffusion on lawsonite $\delta^{18}O$.

An additional important consideration is the tectonic setting of exhumed lawsonite-bearing rocks. The occurrence of lawsonite-bearing HP/LT rocks in exhumed subduction complexes is commonly characterized by meters-scale blocks within mélange domains (Endo et al., 2012; Krebs et al., 2011; Wakabayashi, 2015) or as kilometer-scale, structurally more coherent units (Harvey et al., 2021; Martin et al., 2011; Vitale Brovarone & Herwartz, 2013; Whitney et al., 2014). However, there are some cases in which the distinction between blocks in mélange and structurally coherent units becomes challenging. This ambiguity arises (a) where mélange areas interfinger with coherent units at a local scale (Vitale Brovarone et al., 2018; Wakabayashi, 2015), (b) where the preferential weathering of mélange matrix has created isolated exposures of blocks that lack clear geological context (Krogh et al., 1994), and (c) where HP/LT rocks were exhumed as xenoliths in diatremes (Hernández-Uribe & Palin, 2019; Usui et al., 2003, 2006).

Extensive research has been focused on mélange domains to investigate element transfer along the slab-mantle interface owing to the ample evidence of fluid-rock interactions in the highly deformed mélange matrix (Errico et al., 2013; Penniston-Dorland et al., 2010). In contrast, the role of more structurally coherent HP/LT terranes has received less attention, and these terranes have, in some cases, been interpreted as compositionally closed systems (Collins et al., 2015; Spandler et al., 2011). However, the presence of HP veins and metasomatic reaction zones indicate that some coherent terranes experienced extensive metasomatism (Fornash & Whitney, 2020; Piccoli et al., 2018; Vitale Brovarone et al., 2014).

This study aims to track fluid-rock interactions and the sources of fluids in subduction complexes using the oxygen isotope composition of lawsonite in exhumed HP/LT rocks. We targeted lawsonite from mélange domains (Port Macquarie/Australia; Rio San Juan/Dominican Republic; South Motagua/Guatemala; Franciscan/USA), from more structurally coherent units (Catalina/USA; Diahot/New Caledonia; Alpine Corsica/France; Tavşanlı/Turkey), from isolated eclogite blocks (Pinchi Lake/Canada complex), and from one diatreme (Garnet Ridge/USA). Garnet coexisting with lawsonite was additionally analyzed for its oxygen isotope composition in some samples. To differentiate the influence of fluid-related factors on $\delta^{18}O_{Lws}$, we evaluated the temperature influence on $\delta^{18}O_{Lws}$ and $\delta^{18}O_{Grt}$, and the contribution of intracrystalline diffusion to $\delta^{18}O_{Grt}$ as a way of assessing the same effect on $\delta^{18}O_{Lws}$. Relationships between water/rock (W/R) ratio and the $\delta^{18}O$ of fluid that formed lawsonite-bearing metasomatites from two structurally coherent terranes (Tavşanlı/Turkey; Alpine Corsica/France) were also investigated using Monte Carlo simulations. Therefore, this study presents a new method for tracking fluid-rock interactions and fluid sources in subduction complexes using the novel method of lawsonite oxygen isotope composition in concert with other geochemical indicators.

2. Geology and Sample Descriptions

The general field relations of the 10 subduction complexes are briefly summarized along with textural descriptions of the samples. A detailed description of the samples is provided in Text S1 of the Supporting Information S1.

2.1. Port Macquarie, Eastern Australia (Serpentinite-Matrix Mélange)

In the Port Macquarie mélange, a serpentinite-matrix surrounds two large (~100 m scale) bodies of chlorite-actinolite schist that enclose blocks of blueschist, eclogite, chert, marble, omphacitite, and massive serpentinite. Lawsonite-bearing HP/LT metabasalts mostly occur as blocks, some of which consist of alternating mm- to cm-scale blueschist and eclogite layers. Lawsonite eclogite records peak P-T conditions of 590°C, ~2.7 GPa with an age of 490 Ma, whereas lawsonite-garnet blueschist records slightly lower peak P-T conditions (550°C, ~2.0 GPa) with an age of 470–460 Ma (Fukui et al., 1995; Och et al., 2003; Tamblyn, Hand, Kelsey, et al., 2020).

Samples 17RB-22 and 17RB-3C are from a metabasalt composed of alternating mm- to cm-scale layers of blueschist and eclogite (Figure 1a). Lawsonite in eclogite (17RB-22) occurs either as inclusions in garnet or in texturally late phengite- or chlorite-rich domains (Figure 1b). Garnet in the texturally late domains contains lawsonite and epidote as inclusions. Lawsonite in blueschist (17RB-3C) occurs in the matrix and as inclusions in garnet.

2.2. Rio San Juan Complex, Dominican Republic (Serpentinite-Matrix Mélange)

Serpentinite-matrix mélanges occur in the northern part of the Rio San Juan complex and contain blocks of various rock types (e.g., serpentinite, blueschist, eclogite, marble) (Krebs et al., 2011). Although very rare lawsonite eclogite occurs in these mélange bodies (Thomas et al., 2004), lawsonite primarily occurs in blueschist-facies rocks that record peak P-T conditions of 360–370°C and 1.6–1.7 GPa with ages of 62.1–71.9 Ma (Krebs et al., 2008, 2011). Sample IEC15–3.5 is from a blueschist-facies metamafic boulder that contains lawsonite in the matrix. This sample is interpreted as a metagabbro owing to the coarse-grained major matrix phases (Kang et al., 2022).

2.3. South Motagua Fault Zone, Guatemala (Serpentinite-Matrix Mélange)

The extensive serpentinite mélanges of Guatemala are exposed to major strike-slip faults, such as the South Motagua fault zone (Marroni et al., 2009; Ratschbacher et al., 2009). The South Motagua fault zone contains HP/LT blocks (e.g., lawsonite eclogite and blueschist) and metasomatites (e.g., jadeitite, omphacitite). Lawsonite-bearing HP/LT blocks evolved along a clockwise P-T path, with peak P-T conditions of 480–520°C, 2.5–2.6 GPa (Endo et al., 2012; Tsujimori, Sisson, et al., 2006) and ages of 140–120 Ma (Brueckner et al., 2009; Harlow et al., 2004).

Sample MVE04-7-2 is a lawsonite eclogite, with lawsonite occurring in the matrix and as inclusions in garnet (Figure 1c). Sample 01GSn2-9 is an omphacitite consisting of omphacite, lawsonite, and actinolite with minor amounts of apatite, quartz, and sulfides. Lawsonite in this rock commonly includes chromite.

2.4. Franciscan Complex, California, USA (Serpentinite- and Siliciclastic-Matrix Mélange)

The Franciscan Complex of California is comprised of coherent thrust belts consisting of metabasaltic and metasedimentary rocks, with mélange units that contain HP/LT blocks within a sheared serpentinite- or siliciclastic matrix (Wakabayashi, 2015). High-grade lawsonite-bearing blocks record an anticlockwise P-T path, evolving from epidote-eclogite facies (600–700°C, 0.7–1 GPa) (Ernst & Liu, 1998; Tsujimori, Matsumoto, et al., 2006) to lawsonite-blueschist facies conditions (150–250°C, 0.6–1 GPa) (Brown & Ghent, 1983; Ernst, 1993; Ernst & McLaughlin, 2012). These high-grade blocks reached peak metamorphic conditions between 166 and 140 Ma (Anczkiewicz et al., 2004; Mulcahy et al., 2009, 2014; Page et al., 2007).

We analyzed four samples from three mélange zones in the Franciscan Complex. Samples LVT-1 and RR-1 are from a serpentinite-matrix mélange exposed in the Ring Mountain Preserve in Marin County. Sample LVT-1 is a lawsonite-bearing metabasite composed of alternating mm- to cm-scale blueschist and eclogite layers. Both layers contain lawsonite-rich veins. Sample RR-1 is a blueschist, with lawsonite occurring in the matrix and in a calcite-rich vein. Sample EC-1B is a lawsonite blueschist from a North Berkeley Hills serpentinite-matrix mélange. Lawsonite veins in EC-1B have been partially to completely replaced by chlorite and pumpellyite. Sample SM-8 is from a small (~35 cm wide) lawsonite blueschist block from a siliciclastic-matrix mélange at Blind Beach (Sonoma County).

10.1029/2023GC011389

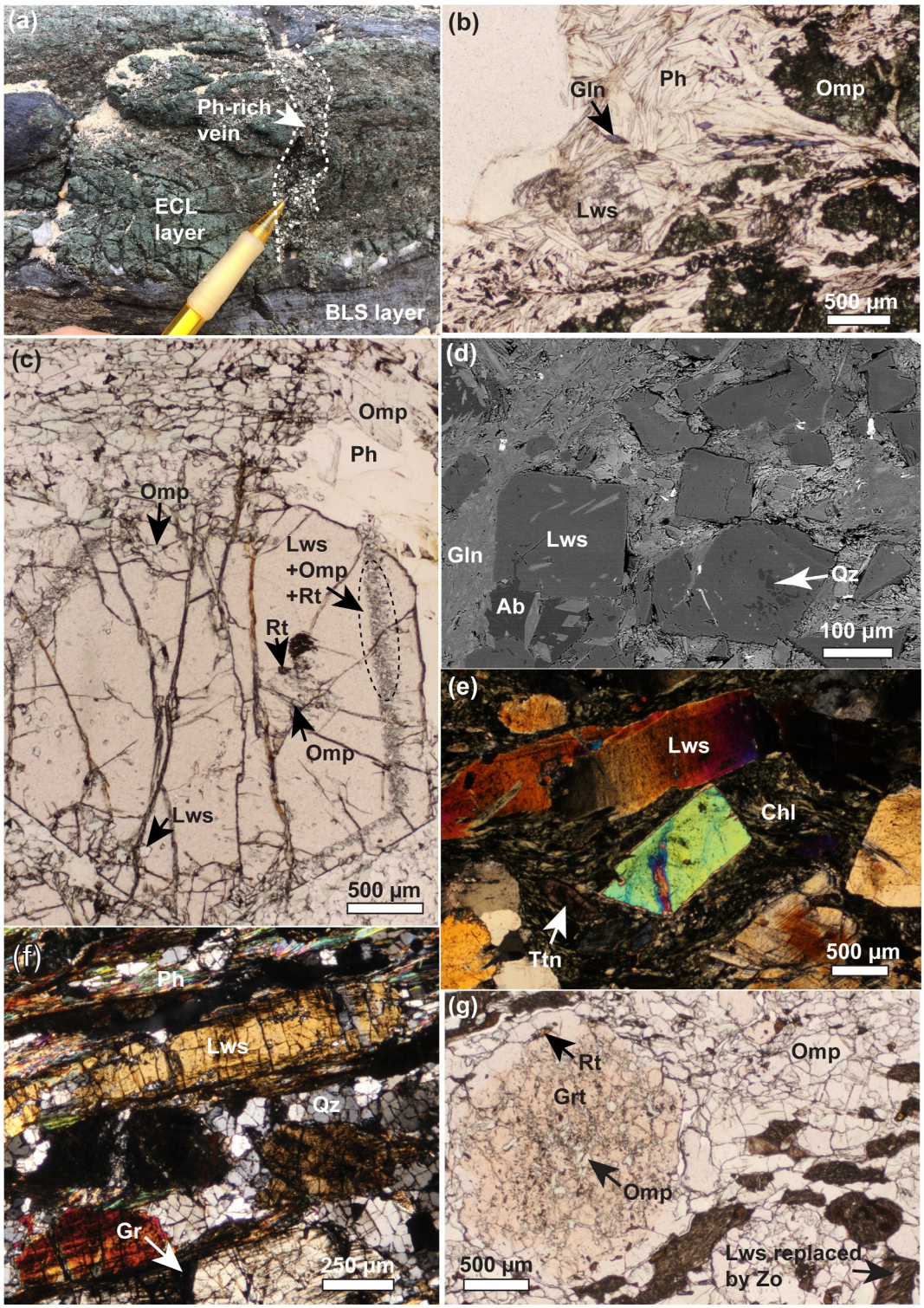

Figure 1. (a, b) Images of interlayered metabasalt from the Port Macquarie serpentinite-matrix mélange (17RB-3C, 22), showing alternating blueschist (BLS) and eclogite (ECL) layers (a; outcrop) and lawsonite in texturally later domains (e.g., phengite-rich vein) (b; PPL). (c) Photomicrograph of lawsonite-bearing eclogite from the South Motagua serpentinite-matrix mélange (MVE04-7-2) (c; PPL). (d) BSE Image of lawsonite-bearing blueschist-facies metagabbro from the structurally coherent Diahot terrane (NC19-159). (e, f) Photomicrographs of lawsonite-bearing metasomatites from the structurally coherent Alpine Corsica (e, f; XPL). One sample has a higher lawsonite mode (COR18-PK3 with >75 vol%; e) than the other sample (COR18-PK4 with ~25 vol%; f). (g) Photomicrograph of eclogite-facies xenolith from the Garnet Ridge/Colorado Plateau (g; PPL). Note that lawsonite has been partially replaced by fibrous aggregates of zoisite. Mineral abbreviations follow Whitney and Evans (2010).

2.5. Catalina Schist, Santa Catalina Island, California, USA (Structurally Coherent)

The Catalina Schist is largely composed of meter- to kilometer-scale coherent units, primarily consisting of metagreywacke and metapelite. These coherent units are locally associated with highly sheared zones, including mélange zones. The highest-grade, amphibolite-facies mélange preserves records of metasomatic reactions; it contains a range of rock types (e.g., quartzite, metapelite, ultramafic/mafic rocks) as blocks in a matrix of mixed ultramafic and mafic material (Bebout & Barton, 1993, 2002; King et al., 2006).

Lawsonite-bearing blueschist is the most abundant rock type of the Catalina HP/LT complex and it primarily occurs as coherent units that reached peak conditions of ∼350°C, ∼0.8–1.2 GPa (Grove & Bebout, 1995; Grove et al., 2008; Penniston-Dorland & Harvey, 2023) at ∼116–106 Ma (Grove & Bebout, 1995; Grove et al., 2008; Penniston-Dorland & Harvey, 2023). We analyzed two lawsonite blueschist-facies metabasalts: one with garnet (B16-006) and one without garnet (B16-011).

2.6. Diahot Complex, New Caledonia (Structurally Coherent)

The Diahot Complex is part of the New Caledonia blueschist-to-eclogite facies sequence (Clarke et al., 1997). It dominantly consists of coherent metasedimentary units (metagreywacke and metapelite) that also contain layers of metabasalt and metafelsic volcanic rocks (Clarke et al., 1997; Fitzherbert et al., 2005). In the HP/LT complex as a whole, including the adjacent Pouébo terrane HP/LT rocks (e.g., epidote eclogite), these lithologies are locally interleaved with serpentinite along 100 m-scale sheared domains (Rawling & Lister, 2002; Vitale Brovarone et al., 2018).

HP/LT rocks of the Diahot Complex record a range of P-T conditions, from ∼360°C, ∼0.7–0.9 GPa near the lawsonite-in isograd to ∼540°C, 1.0–1.2 GPa near the lawsonite-out (epidote-in) zone (Clarke et al., 1997; Vitale Brovarone & Agard, 2013) with an age of ∼40 Ma (Baldwin et al., 2007; Cluzel et al., 2010; Vitale Brovarone et al., 2018). Sample NC19-159 (IGSN: IENHR005V) is a lawsonite-bearing blueschist interpreted as a metagabbro based on its textures (Figure 1d).

2.7. Alpine Corsica, France (Structurally Coherent)

In Alpine Corsica, lawsonite-bearing HP/LT rocks are exposed as stacked coherent units (Vitale Brovarone & Herwartz, 2013). In addition, lawsonite occurs within calc-schist associated with eclogite and within metasomatite at the contact of serpentinite with metasedimentary rocks (Martin et al., 2011; Piccoli et al., 2018). Lawsonite also occurs in omphacite-rich rocks (omphacitite) hosted by metagabbro (Vitale Brovarone, 2013). Lawsonite-bearing HP/LT units decrease in age structurally downwards from metasediment-richer blueschist units (350–460°C, 1.5–1.8 GPa, 36–38 Ma) to metaophiolite-richer eclogite units (490–550°C, 2.2–2.4 GPa, 33–36 Ma) (Martin et al., 2011; Ravna et al., 2010; Vitale Brovarone & Herwartz, 2013; Vitale Brovarone et al., 2011). Eclogite-facies lawsonite-bearing metasomatites have been interpreted to have formed during subduction metamorphism at 350–550°C, 1.5–2.3 GPa (Vitale Brovarone et al., 2014).

We analyzed three samples of lawsonite-bearing rocks from this complex. Sample C13 is a metagabbro that mainly consists of omphacite and lawsonite. Samples COR18-PK3 and COR18-PK4 are lawsonite-bearing metasomatites with different lawsonite modes (>75 vol%; ∼25 vol%, respectively) (Figures 1e and 1f). COR18-PK3 contains abundant chlorite (Figure 1e) and COR18-PK4 contains quartz and graphite (Figure 1f). In COR18-PK4, lawsonite also occurs in quartz veins.

2.8. Tavşanlı Zone, Turkey (Structurally Coherent)

The Tavşanlı Zone is an HP/LT belt characterized by interlayered metasedimentary and metabasaltic coherent units (Okay, 1980, 1982, 1986; Plunder et al., 2015). Marble and calcschist are dominant lithologies relative to quartzite and metabasite. We analyzed six samples from the Tavşanlı Zone (TZ), including five from the Sivrihisar Massif (SV), which is the lawsonite eclogite-bearing part of the Tavşanlı Zone. In the Sivrihisar Massif, lawsonite occurs in all lithologies except pure marble. The structurally coherent units of lawsonite blueschist contain layers and pods of lawsonite eclogite. Lawsonite also occurs in chlorite ± garnet-rich metasomatite at the contact of serpentinite lenses with metabasite and metasediment. The HP/LT rocks record prograde-to-peak P-T conditions of 380–550°C, 1.2–2.4 GPa (Davis & Whitney, 2006, 2008; Kang et al., 2020; Pourteau et al., 2019) with ages of 105–83 Ma (Fornash et al., 2016; Mulcahy et al., 2014; Pourteau et al., 2019); eclogites are older than

the dated blueschists, indicating that at least some blueschists are retrograde (Fornash et al., 2016; Mulcahy et al., 2014).

Samples were analyzed from 6 lawsonite-bearing rock types: an eclogite (SV08-283C); a lawsonite + garnet blueschist (SV01-75A); a metabasite with alternating fine-scale blueschist and eclogite layers, both of which contain lawsonite in the matrix and in calcite veins (SV01-50A); a lawsonite + chlorite-rich metasomatic block (TZ10-2.2C); a lawsonite + garnet-bearing quartzite (SV08-281D); and a lawsonite-bearing calc-schist (SV08-7ADD). Some garnet grains in SV01-75A have been extensively replaced by chlorite.

2.9. Pinchi Lake, British Columbia, Canada (Boulders)

In the Pinchi Fault Zone, lawsonite occurs in eclogite boulders that show no clear field relations with the surrounding rocks, although these boulders have been interpreted as part of a mélange (Ghent et al., 1996, 2009). Eclogite blocks are in the same HP/LT complex as carbonate-bearing coherent blueschist units, and both eclogite and blueschist have similar cooling ages (223–211 Ma) (Ghent et al., 1996; Paterson & Harakal, 1974). Lawsonite eclogite blocks record peak P-T conditions that slightly differ from each other depending on the extent of retrogression; least retrogressed eclogite: 450°C, 2.5 GPa; retrogressed eclogite: 570°C, >1.3 GPa (Ghent et al., 1993, 2009). Analyzed samples are from a retrogressed eclogite (BLR4) and a relatively fresh eclogite (BLR5), both of which contain lawsonite in the matrix and as inclusions in garnet. Lawsonite also occurs in a phengite-rich vein in BLR5.

2.10. Garnet Ridge Diatreme, Navajo Volcanic Field, Arizona, USA (Xenolith)

More than 50 diatremes are exposed in the Navajo Volcanic Field in the central Colorado Plateau; three (including Garnet Ridge) contain lawsonite-bearing xenoliths (Atwater, 1970; Dickinson, 1997). These xenoliths are surrounded by brecciated fragments of serpentinized ultramafic rocks and experienced lawsonite eclogite-facies metamorphism (560–700°C at 3 GPa; 600–760°C at 5 GPa) at 81–33 Ma (Hernández-Uribe & Palin, 2019; Smith et al., 2004; Usui et al., 2003). Subsequent recrystallization partially decomposed lawsonite into fine aggregates of fibrous zoisite (Usui et al., 2003, 2006).

Sample 17GR11 is a lawsonite-bearing eclogite xenolith from the Garnet Ridge diatreme. It is composed of garnet, omphacite, and lawsonite partially replaced by fibrous zoisite aggregates, with minor amounts of rutile and pyrite (Figure 1g; see also Figure 2 in Hernández-Uribe & Palin, 2019). Garnet contains inclusions of omphacite, lawsonite rimmed by fibrous zoisite aggregates, and rutile.

3. Analytical Methods

3.1. Major and Minor Element Compositions

Major and minor element compositions of lawsonite and garnet were analyzed with a JEOL JXA-8530F Plus Electron Probe Microanalyzer in the Department of Earth and Environmental Sciences at the University of Minnesota. A 15 kV accelerating voltage and a 20 nA beam current were used for quantitative analyses, with a focused beam for garnet and a defocused 10 μm for lawsonite. X-ray element maps of lawsonite and garnet were acquired using a 15 kV accelerating voltage, a 100 nA beam current, a focused beam, and a dwell time of 10 ms. A step size (0.3–3 μm) was adjusted depending on grain size.

3.2. Oxygen Isotope Compositions

The oxygen isotope ratio ($^{18}O/^{16}O$) of lawsonite and garnet was determined by SIMS using a Cameca 1280 multi-collector ion probe at the Center for Microscopy, Characterization and Analysis, University of Western Australia. Samples were mounted as thin section cuts or polished rock chips in a 25 mm diameter epoxy disk, together with matrix-matched standards of lawsonite and garnet.

Both lawsonite and garnet were analyzed using the same analytical protocol. In situ oxygen isotope analyses were performed using a Gaussian Cs^+ beam, focused to a 15 μm spot on the sample surface, with a beam intensity of ~2.5–3 nA and a total impact energy of 20 keV. Each analysis consists of a 20 4-s cycle acquisition. The analytical session of lawsonite was monitored for drift and precision by analyzing two lawsonite bracketing standards every 5–6 sample analyses. Instrumental mass fractionation (IMF) was corrected using the matrix-

matched reference materials, including SHB32 as a primary standard (LF $\delta^{18}O_{VSMOW} = 13.4 \pm 0.2‰$, $n = 3$) and LW-C as a secondary standard (LF $\delta^{18}O_{VSMOW} = 8.68 \pm 0.2‰$, $n = 2$).

To monitor the stability of garnet analytical sessions, one garnet standard (UWG-2) was analyzed twice every 5–6 garnet sample analyses. For each mount, 6 garnet standards with different grossular compositions (X_{Grs}) were measured at the beginning, middle, and end of the analytical session to account for the matrix effect of X_{Grs} on the measurement bias of $\delta^{18}O_{Grt}$ (e.g., Martin, Rubatto, et al., 2014; Page et al., 2010; Vielzeuf et al., 2005). The relationship between the bias and X_{Grs} of all mounts was fitted with a parabolic curve, returning a regression residual of ~0.3‰, which is within the external reproducibility observed on UWG-2. The garnet reference materials used in this study include 10,691, 2B3, GRS-SE, and UWG2 (Eiler et al., 1997; Kohn & Valley, 1998; Valley et al., 1995) and ALM-GEM (in house, $X_{Grs} = 0.01$, $\delta^{18}O = 6.79‰$). The reproducibility of the lawsonite and garnet primary standards was better than 0.43‰ (2σ) and 0.57‰ (2σ), respectively, across all sessions.

The oxygen isotope analyses of lawsonite and garnet samples were acquired within the same element zoning domain of the spot locations where electron microprobe measurements were performed for matrix correction (within <120 μm). Further details of the analytical methods are presented in Text S2 of the Supporting Information S1. Complete oxygen isotope analyses (raw $^{18}O/^{16}O$ ratios and $\delta^{18}O$ reported with respect to Vienna Standard Mean Ocean Water) are provided in Table S1 of the Supporting Information S2.

4. Analytical Results

In the following sections, we document the major/minor element composition, zoning patterns of major/minor elements, and oxygen isotope composition of lawsonite and garnet in the subduction sample suite.

4.1. Lawsonite Composition

Analyzed lawsonite grains are from diverse textural sites (e.g., in garnet, matrix, vein), and are largely unaltered, without textural evidence for replacement except for those in the Garnet Ridge xenolith (17GR11; Figure 1g). Some lawsonite grains were previously analyzed and reported for their major and minor element compositions (Kang et al., 2022); therefore, these grains are only briefly discussed in the following sections.

4.1.1. Transition Metal Element Concentrations

Notwithstanding different lithologies, textural sites, and zoning patterns, lawsonite grains analyzed in this study incorporate Fe and Ti at the weight percent level (up to 3.5 wt% Fe_2O_3*; up to 1.7 wt% TiO_2) in addition to Ca and Al as major components (Table 1 and Table S2 in Supporting Information S2). Most grains contain less Cr (<1 wt %), with the exception of the chromite-bearing lawsonite in the S. Motagua fault zone (FZ) omphacitite (01GSn2-9), which has a significantly high Cr-content (3.4–14.3 wt%) (Figure 2a and Table 1). Vein-lawsonite in some Franciscan metabasalts (Ring Mt. interlayered blueschist/eclogite LVT-1, N. Berkeley Hills blueschist EC-1B) and matrix lawsonite in Corsica metasomatites (COR18-PK3, 4) are higher in Cr- and Ti-contents than matrix lawsonite in host- and/or adjacent rocks (Figure 2a). A negative correlation (Pearson's $r \leq -0.71$) is observed between Fe and Al + Cr + Ti in ~36% of our compiled compositional analyses (Figure 2b).

4.1.2. Fe, Ti, and Cr Zoning Patterns

The analyzed grains display characteristic zoning patterns in Fe, Ti, and Cr, which vary among different sample locations, samples, and individual grains even when occurring in the same textural site within the same lithology (e.g., matrix grains in different blueschists) (Table 1, Table S2 in Supporting Information S2). Despite such variations, our compilation of Fe, Ti, and Cr zoning patterns shows that concentric zoning is common, with enrichment of these elements either at the core or rim (Figure 3a and Table 1), regardless of textural site and lithology.

Some grains exhibit Ti-hourglass sector zoning (Table 1), which is characterized by up to four different domains that vary in Ti content (Vitale Brovarone et al., 2014): Zone 1: Ti-intermediate core; Zone 2: Ti-rich mantle; Zone 3: Ti-poor rim; Zone 4: variable Ti-content with oscillatory Cr-zoning (Figure 3b; see also Figure 8e in Kang et al., 2022). Zones 1 and 4 are preserved in some but not all of the analyzed grains.

Geochemistry, Geophysics, Geosystems

10.1029/2023GC011389

Table 1
Representative Compositions and Zoning Patterns of Lawsonite

	Zoning patterns					Fe_2O_3* (wt%)	TiO_2 (wt%)	Cr_2O_3 (wt%)
	Fe		Ti	Cr				
Serpentinite-matrix mélange								
Port Macquarie, Australia								
17RB-22 (ECL layer of interlayered BLS/ECL)	Lws in Grt	Core to rim	Irregular	——	Min	0.58	b.d.l.	b.d.l.
					Max	1.10	0.91	0.13
					Avg	0.77	0.37	0.04
					Fe-poor core*	0.62	0.70	b.d.l.
	Lws in Chl-rich domain	——	Irregular	——	Min	0.51	0.05	b.d.l.
					Max	1.05	1.65	b.d.l.
					Avg	0.78	0.30	b.d.l.
	Lws in Ph-rich domain	Core to rim	Irregular	——	Min	0.31	0.03	b.d.l.
					Max	0.66	0.35	0.05
					Avg	0.52	0.17	0.01
					Fe-poor core*	0.31	0.35	b.d.l.
17RB-3C (BLS layer of interlayered BLS/ECL)	Lws in Grt	Core to rim, Irregular	Core to rim, Irregular	——	Min	0.62	0.03	b.d.l.
					Max	1.24	0.51	0.06
					Avg	0.87	0.16	0.01
					Fe-poor core*	0.69	0.31	b.d.l.
	Matrix Lws	Core to rim	Irregular	——	Min	0.52	b.d.l.	b.d.l.
					Max	2.60	1.06	0.08
					Avg	0.81	0.21	0.02
					Fe-poor core*	0.57	0.07	0.06
Rio San Juan, Dominican Republic								
IEC15–3.5 (BLS-facies metagabbro)	Matrix Lws	Irregular	Irregular	——	Min	0.28	b.d.l.	b.d.l.
					Max	0.66	0.42	0.06
					Avg	0.38	0.12	b.d.l.
South Motagua, Guatemala								
MVE04-7-2 (ECL)	Matrix Lws	Core to rim, Patchy	Patchy	Irregular, ——	Min	0.46	0.03	b.d.l.
					Max	0.98	0.21	0.21
					Avg	0.66	0.09	0.06
					Fe-rich core*	0.79	0.09	0.08
01GSn2-9 (Omphacitite)	Matrix Lws	Irregular, ——	Core to rim, Irregular	Core to rim, Irregular	Min	0.35	0.05	3.42
					Max	0.71	0.67	14.3
					Avg	0.51	0.17	8.33
					Cr-rich core*	0.44	0.23	11.0

Geochemistry, Geophysics, Geosystems

10.1029/2023GC011389

Table 1
Continued

	Fe	Ti	Cr		Fe_2O_3* (wt%)	TiO_2 (wt%)	Cr_2O_3 (wt%)
	Zoning patterns						
Ring Mt., Franciscan Complex							
LVT-1 (Interlayered BLS/ECL)	Matrix Lws	Core to rim	Hourglass-sector	——	Min	0.49	b.d.l.	b.d.l.
					Max	1.12	0.51	0.07
					Avg	0.87	0.08	0.03
	Vein-Lws	Hourglass-sector, ——	Hourglass-sector	Irregular	Min	0.47	b.d.l.	b.d.l.
					Max	1.36	0.57	0.27
					Avg	0.85	0.13	0.12
RR-1 (BLS)	Matrix Lws	Oscillatory	Oscillatory	——	Min	0.48	b.d.l.	b.d.l.
					Max	1.07	1.57	b.d.l.
					Avg	0.68	0.31	b.d.l.
	Lws in Cal-vein	Core to rim	Core to rim	——	Min	0.37	0.63	b.d.l.
					Max	0.42	0.74	b.d.l.
					Avg	0.39	0.68	b.d.l.
N Berkeley Hills, Franciscan Complex							
EC-1B (BLS)	Matrix Lws	Core to rim	——	——	Min	1.10	0.02	b.d.l.
					Max	1.97	0.09	0.07
					Avg	1.39	0.04	0.04
	Vein-Lws	Core to rim, Oscillatory, Patchy	Patchy, Irregular	Core to rim, Irregular	Min	0.62	b.d.l.	b.d.l.
					Max	2.52	0.72	0.32
					Avg	1.60	0.17	0.13
Siliciclastic-matrix mélange							
Blind Beach, Franciscan Complex							
SM-8 (BLS)	Matrix Lws	Core to rim, Irregular	Irregular	Core to rim, Irregular	Min	0.69	b.d.l.	b.d.l.
					Max	3.00	0.74	0.21
					Avg	1.53	0.19	0.06
Structurally coherent terrane							
Catalina Schist, Santa Catalina Island							
B16-011 (BLS)	Matrix Lws	Core to rim	Core to rim, Patchy	——	Min	0.64	b.d.l.	b.d.l.
					Max	2.94	0.64	0.05
					Avg	1.67	0.23	0.01
B16-006 (Grt-bearing BLS)	Matrix Lws	Oscillatory	Irregular	——	Min	0.22	b.d.l.	b.d.l.
					Max	1.09	0.80	0.07
					Avg	0.67	0.15	0.01

Geochemistry, Geophysics, Geosystems

10.1029/2023GC011389

Table 1
Continued

	Fe	Ti	Cr		Fe_2O_3* (wt%)	TiO_2 (wt%)	Cr_2O_3 (wt%)
	Zoning patterns						
Diahot terrane, New Caledonia							
NC19-159 (BLS-facies metagabbro)	Matrix Lws	Core to rim, Oscillatory	Hourglass-sector	Core to rim	Min	0.30	b.d.l.	b.d.l.
					Max	0.92	0.79	0.21
					Avg	0.49	0.25	0.08
Alpine Corsica, France								
C13 (Lws-Omp metagabbro)	Matrix Lws	Core to rim	Core to rim	——	Min	0.69	0.03	b.d.l.
					Max	1.42	0.37	b.d.l.
					Avg	0.95	0.10	b.d.l.
COR18-PK3 (Metasomatite w/ Lws ~25%)	Matrix Lws (Zone1)	Core to rim	Hourglass-sector, Irregular	Core to rim	Min	0.28	b.d.l.	b.d.l.
					Max	0.41	0.03	0.11
	Matrix Lws (Zone2)				Min	0.26	b.d.l.	b.d.l.
					Max	0.62	0.56	0.10
	Matrix Lws (Zone3)				Min	0.41	0.03	0.05
					Max	0.59	0.04	0.12
COR18-PK4 (Metasomatite w/ Lws >75%)	Matrix Lws (Zone1)	Core to rim, Irregular	Hourglass-sector, Irregular	——	Min	0.19	0.04	b.d.l.
					Max	0.24	0.09	b.d.l.
	Matrix Lws (Zone2)				Min	0.14	0.06	b.d.l.
					Max	0.40	1.49	0.06
	Matrix Lws (Zone3)				Min	0.19	b.d.l.	b.d.l.
					Max	0.37	0.08	b.d.l.
	Lws in Qz-vein	Irregular	Irregular	Irregular, ——	Min	0.12	0.01	b.d.l.
					Max	0.42	1.41	0.07
					Avg	0.25	0.47	0.01
Tavşanlı, Turkey								
SV08-283C (ECL)	Matrix Lws	Irregular	Irregular	——	Min	1.26	0.05	b.d.l.
					Max	3.53	0.24	0.08
					Avg	1.56	0.14	0.02
SV01-75A (BLS)	Matrix Lws	Hourglass-sector, Oscillatory	Hourglass-sector	Oscillatory	Min	1.21	0.03	b.d.l.
					Max	1.73	1.16	1.00
					Avg	1.53	0.32	0.24
SV01-50A (Interlayered BLS/ECL)	Matrix Lws	Core to rim	Core to rim, Irregular	Core to rim, ——	Min	1.17	b.d.l.	b.d.l.
					Max	1.72	0.51	0.07
					Avg	1.37	0.24	0.02

Geochemistry, Geophysics, Geosystems

10.1029/2023GC011389

Table 1
Continued

	Fe	Ti	Cr		Fe_2O_3* (wt%)	TiO_2 (wt%)	Cr_2O_3 (wt%)
	Zoning patterns						
	Lws in Cal-vein			Min	1.01	0.06	b.d.l.
				Max	1.95	0.49	0.15
				Avg	1.53	0.21	0.03
TZ10-2.2C (Metasomatite)	Matrix Lws	Irregular	Irregular	——	Min	0.85	b.d.l.	b.d.l.
					Max	1.89	0.69	0.07
					Avg	1.35	0.11	0.01
SV08-281D (Quartzite)	Matrix Lws	Core to rim	Irregular	Core to rim, Irregular	Min	1.33	0.03	b.d.l.
					Max	2.17	1.01	0.06
					Avg	1.58	0.10	0.01
					Fe-poor core*	1.60	0.05	0.06
SV08-7ADD (Calschist)	Matrix Lws	Core to rim, Irregular	Irregular, ——	Irregular	Min	0.16	0.03	b.d.l.
					Max	0.41	0.41	0.15
					Avg	0.27	0.08	0.04
					Fe-poor core*	0.21	0.06	0.03
Boulders								
Pinchi Lake, British Columbia								
BLR5 (ECL)	Matrix Lws	Core to rim. Irregular	Core to rim, Irregular	Core to rim, Irregular	Min	0.73	b.d.l.	b.d.l.
					Max	2.44	0.40	0.13
					Avg	0.99	0.10	0.04
	Lws in Ph-rich vein	Oscillatory	Core to rim	Core to rim	Min	0.58	b.d.l.	b.d.l.
					Max	0.85	0.83	0.15
					Avg	0.73	0.30	0.07
BLR4 (Retrogressed ECL)	Lws in Grt	Irregular	Core to rim, Irregular	Irregular	Min	0.52	0.03	0.10
					Max	0.67	0.22	0.14
					Avg	0.60	0.12	0.12
	Matrix Lws	Core to rim, Oscillatory, Irregular	Irregular	Core to rim, Oscillatory, Irregular	Min	0.13	b.d.l.	b.d.l.
					Max	0.88	0.89	0.28
					Avg	0.56	0.15	0.08
Xenolith								
Garnet Ridge, Colorado Plateau								
17GR11 (ECL-facies xenolith)	Matrix Lws	Irregular	Irregular	Irregular	Min	0.38	0.07	37.49
					Max	1.88	0.18	38.79
					Avg	0.99	0.13	38.07

Note. Fe_2O_3* = all iron reported in Fe_2O_3 wt%; b.d.l. = less than detection limit; —— = analyzed but not detected; * = average composition of lawsonite with concentric zoning at the core.

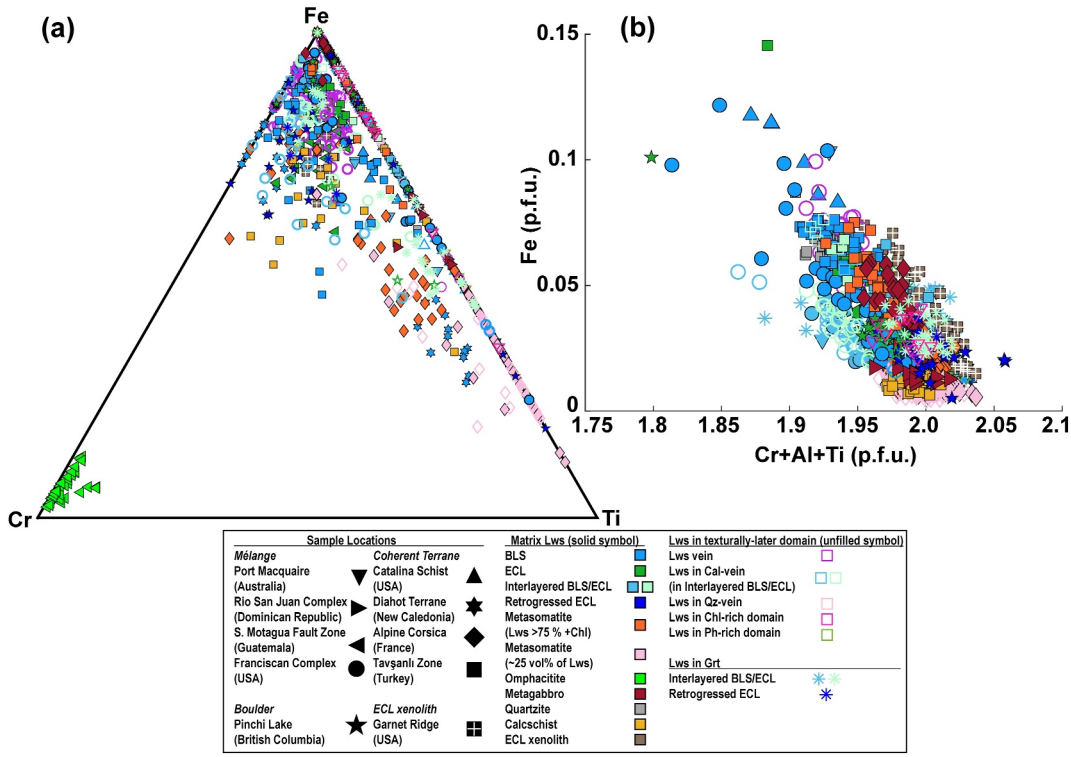

Figure 2. (a) Fe, Ti, and Cr ternary diagrams showing the relative abundance of these elements (in atoms per formula unit; p.f.u.) in lawsonite from 17 blueschist- to eclogite-facies metabasites, 2 metasediments, 4 metasomatites, and 1 eclogite-facies xenolith. (b) Fe^{3+} versus Cr + Al + Ti in lawsonite. Filled symbols indicate matrix lawsonite, unfilled symbols indicate lawsonite in texturally later domain (e.g., vein), and colored asterisks indicate lawsonite included in garnet. Symbols other than asterisks represent different subduction complexes, with different colors indicating different rock types of lawsonite-bearing host rocks or different texturally later lawsonite-bearing domains.

Fe-oscillatory zoning is observed in some matrix grains and vein-lawsonite (Figure 3c and Table 1). Analyzed matrix grains from two Sivrihisar metasediments (quartzite SV01-281D, calc-schist SV08-7ADD) display concentric Fe- and/or Cr-zoning similar to those in metabasaltic layers in close proximity (e.g., interlayered blueschist/eclogite SV01-50A; Table 1). Distinctive Ti-zoning patterns are observed in Corsica metasomatic lawsonite (e.g., hourglass sector zoning or irregular patchy zoning; COR18-PK3, 4) as compared to Corsica metagabbro lawsonite (concentric zoning; C13) (Table 1).

4.1.3. Oxygen Isotope Compositions

Lawsonite in fine-grained blueschist- to eclogite-facies metabasalts (7.6 ± 0.2–14.8 ± 1.1‰, n = 309, 14 samples) records isotopically lighter $\delta^{18}O$ than that in metasediments (20.6 ± 1.4–24.1 ± 1.3‰, n = 25, 2 samples), but its $\delta^{18}O$ value overlaps with the upper range of lawsonite in coarser-grained metamafic rocks that are inferred to be metagabbro (4.0 ± 0.4–7.9 ± 0.3‰, n = 36, 3 samples) (Figure 4 and Table 2). Metasomatite lawsonite from the S. Motagua FZ mélange (omphacitite 01GSn2-9) and the Tavşanlı coherent terrane (TZ10-2.2C) has $\delta^{18}O$ within the range of metabasalt lawsonite from the same locations (S. Motagua FZ eclogite MVE04-7-2; Sivrihisar eclogite SV08-283C, blueschist SV01-75A) (Figure 4 and Table 2). This contrasts with metasomatite lawsonite from the Corsica coherent terrane (COR18-PK3, 4: 11.0 ± 2.0–12.2 ± 1.5‰, n = 40, 2 samples), which is significantly heavier than Corsica metagabbro lawsonite (C13: 4.0 ± 0.4‰, n = 12, 1 sample) (Figure 4 and Table 2).

Lawsonite in metabasalt from more structurally coherent subduction complexes has a similar-to-higher range of $\delta^{18}O$ (11.7 ± 0.4–14.1 ± 1.0‰, n = 76, 5 samples) compared to that from serpentinite- and siliciclastic-matrix mélanges (7.6 ± 0.2–10.3 ± 2.0‰, n = 167, 7 samples). Lawsonite in mélange metagabbro from the Rio San Juan Complex (7.9 ± 0.3‰, n = 9, 1 sample) is close to the upper $\delta^{18}O$ range of lawsonite in coherent terrane

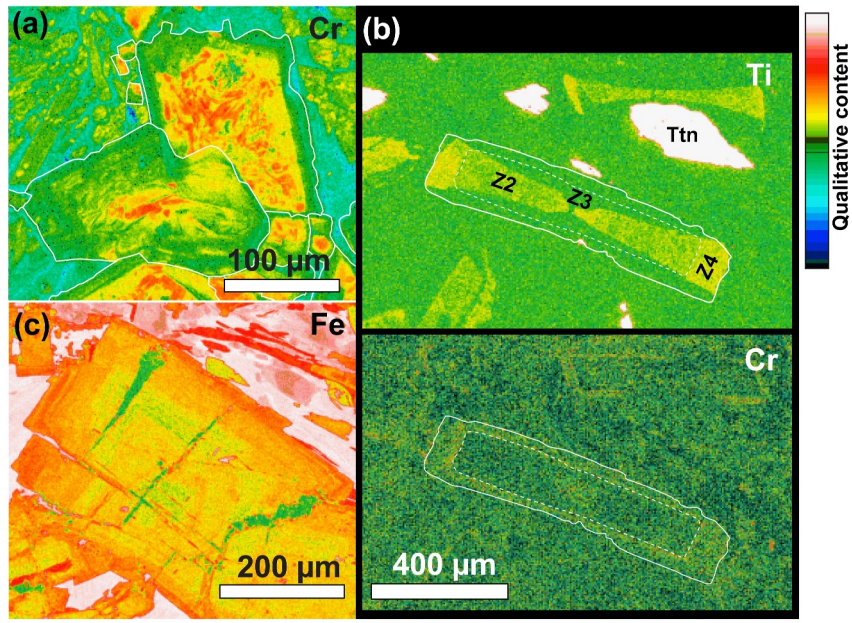

Figure 3. Fe, Ti, and Cr zoning patterns in lawsonite. (a) Cr-concentric zoning with irregular Cr-rich patchy domains at the core of matrix lawsonite (S. Motagua FZ omphacitite 01GSn2-9). (b) Ti-hourglass sector zoning with Ti-rich (Zone 2; Z2), Ti-poor (Zone 3; Z3), and Ti-variable (Zone 4; Z4) domains in matrix lawsonite (Corsica metasomatite COR18-PK3). Note that Zone 4 is Cr-richer than the other domains. (c) Fe oscillatory zoning in vein-lawsonite (N. Berkeley Hills blueschist EC-1B). White solid lines: grain boundaries of lawsonite grains. Dotted white lines: boundaries between Zone 3 and Zone 4.

metagabbro from the Diahot terrane and Alpine Corsica (4.0 ± 0.4–6.4 ± 1.8‰, $n = 27$, 2 samples) (Figure 4 and Table 2).

Approximately 28% of the analyzed lawsonite grains show ~1–1.7‰ variations (>4σ) (Figure 4 and Table 2). These isotopically zoned grains occur in the matrix or vein of S. Motagua FZ eclogite (MVE04-7-2), Ring Mt. blueschist (RR-1), Sivrihisar blueschist (SV01-75A) and calcschist (SV08-7ADD), Tavşanlı metasomatite (TZ10-2.2C), and Pinchi Lake eclogites (BLR4, 5). Notably, vein-lawsonite from N. Berkeley Hills blueschist (EC-1B) and some matrix grains in S. Motagua FZ omphacitite (01GSn2-9), Ring Mt. interlayered blueschist/eclogite (LVT-1), Catalina blueschist (B16-006), Diahot blueschist-facies metagabbro (NC19-159), Corsica metasomatites (COR18-PK3, 4), and Sivrihisar quartzite (SV08-281D) are significantly zoned, showing 2.0–3.8‰ variations (Figure 4 and Table 2). Intergrain (within sample)-scale variation has only been observed for the N. Berkeley Hills blueschist (EC-1B) in which vein-lawsonite is isotopically lighter by ~3‰ compared to matrix lawsonite (Figure 4 and Table 2).

4.2. Garnet Composition

We analyzed matrix garnet from two blueschist layers (Port Macquarie 17RB-3C, Sivrihisar SV01-75A), three eclogite blocks (S. Motagua FZ MVE04-7-2, Sivrihisar SV08-283C, Pinchi Lake BLR5), one eclogite xenolith (Garnet Ridge 17GR11), and one quartzite layer (Sivrihisar SV08-281D). In all but the Sivrihisar blueschist (partially chloritized garnet) and the Garnet Ridge xenolith (lawsonite replaced by fibrous aggregates of zoisite), analyzed garnet is free of textural replacement and in textural equilibrium with matrix lawsonite.

4.2.1. Major and Minor Element Compositions

Except for Mn-rich garnet in the Sivrihisar quartzite (SV08-281D), the analyzed grains from blueschist- to eclogite-facies metabasalts are Ca- and Fe-rich (Table 3 and Table S3 in Supporting Information S2). Garnet within all samples but the S. Motagua FZ eclogite is more enriched in Mn in the core than in the rim (Table 3). An oscillatory-zoned outermost rim is locally preserved on garnet from the Sivrihisar eclogite (SV08-283C) and quartzite (SV01-281D), with the composition of $alm_{51–59}sps_{6–15}prp_{6–14}grs_{23–26}$ and $alm_{<4}sps_{73–82}prp_{6–9}grs_{3–11}$, respectively (Figure 5a and Table 3). This is in contrast to the garnet from other locations (Port Macquarie, S.

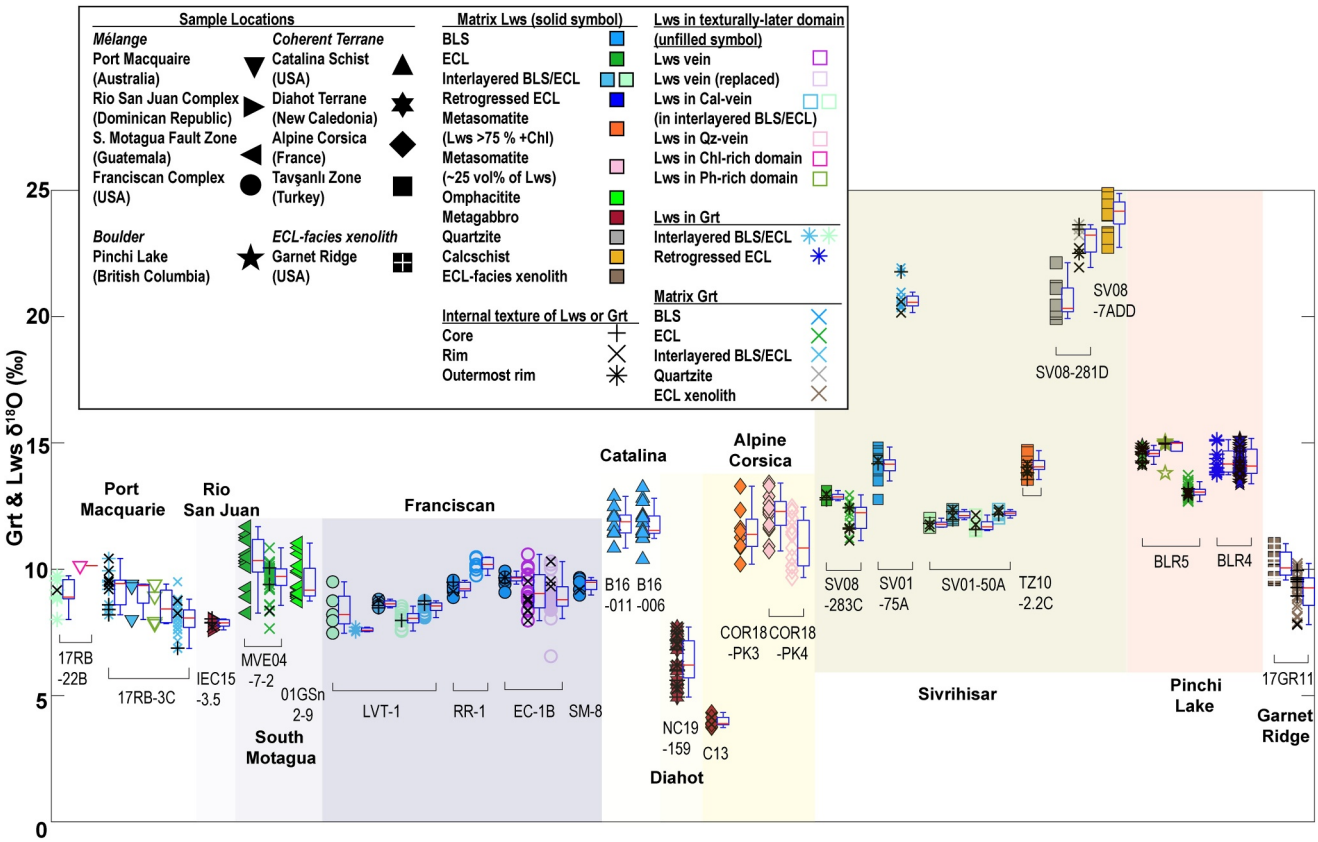

Figure 4. $\delta^{18}O$ of lawsonite and garnet. Each box is marked with the median value of lawsonite or garnet $\delta^{18}O$ analyses on the left, and the bottom and top edges define the 25th and 75th percentiles. Blue whisker lines extend to the most extreme values within the 1.5 interquartile range. Filled symbols indicate matrix lawsonite, unfilled symbols indicate lawsonite in a texturally later domain (e.g., vein), colored asterisks indicate lawsonite included in garnet, and colored "*x*" symbols indicate matrix garnet. Black crosses, "*x*" symbols, and asterisks indicate $\delta^{18}O$ analysis at the core, rim, and outermost rim positions of lawsonite or garnet. Symbols other than crosses, "*x*" symbols, and asterisks represent different subduction complexes, with different colors indicating different lithologies of lawsonite-bearing host rocks or different texturally later lawsonite-bearing domains.

Motagua FZ, and Garnet Ridge), which shows oscillatory zoning in Ca, Fe, and Mg throughout the entire grain (Figures 5b and 5c). The garnets from Port Macquarie and Garnet Ridge show similar zoning patterns in which Ca is negatively correlated with Fe and Mg (Figure 5c). The S. Motagua FZ garnet is oscillatory zoned in Mn in addition to Ca, Fe, and Mg, with Ca oscillating inversely with Mg (Table 3 and Table S3 in Supporting Information S2).

4.2.2. Oxygen Isotope Composition

Garnets in the Sivrihisar quartzite (SV08-281D) and blueschist (SV01-75A) have a higher range of $\delta^{18}O$ (20.7 ± 1.1–23.0 ± 1.2‰, n = 20, 2 samples) than in the other blueschist- to eclogite-facies metabasalts (8.1 ± 1.3–13.1 ± 0.5‰, n = 121, 5 samples) (Figure 4 and Table 2). Only garnet in the Sivrihisar eclogite (SV08-283C) from the structurally coherent Tavşanlı terrane has $\delta^{18}O$ (12.1 ± 1.1‰, n = 15) closer to the range of garnet from the mélanges (Port Macquarie, S. Motagua FZ) (8.1 ± 1.3–9.6 ± 1.3‰, n = 56, 2 samples) (Figure 4 and Table 2).

Garnet in the Sivrihisar eclogite (SV08-283C) and blueschist (SV01-75A) exhibits a core-to-rim decrease in $\delta^{18}O$ (1.3–1.4‰) (Figure 4 and Table 2). A subsequent $\delta^{18}O$ increase (1.3‰) is only observed in the eclogite garnet, and it occurs in the oscillatory-zoned outermost rims (Figure 5d and Table S1 in Supporting Information S2). Garnet in the Sivrihisar quartzite (SV08-281D) shows a gradual decrease in $\delta^{18}O$ toward the rims, but a 1.7‰ decrease is only noticeable in a garnet that preserves the oscillatory outermost rims (garnet 2 in Table 2). Pervasively oscillatory-zoned garnet shows either an overall decrease (S. Motagua FZ eclogite MVE04-7-2: −1.4‰; Garnet Ridge xenolith 17GR11: −1.7‰) or an increase in $\delta^{18}O$ (blueschist layer of Port Macquarie

Geochemistry, Geophysics, Geosystems

10.1029/2023GC011389

Table 2
Lawsonite and Garnet Oxygen Isotope Compositions

Location	Sample	Rock type	Texture	Avg $\delta^{18}O$	2σ	Min $\delta^{18}O$	2σ	Max $\delta^{18}O$	2σ	Core $\delta^{18}O$	2σ	Rim $\delta^{18}O$	2σ	Outermost rim $\delta^{18}O$	2σ
Serpentinite-matrix mélange															
Rocky Beach, Port Macquarie	17RB-22	Interlayered BLS/ECL	Lws in Grt (ECL)	9.1	1.1	8.0	0.7	9.7	0.7	9.2[a]	0.9	8.6[a]	1.6		
			Lws in Chl-rich domain (ECL)			10.1[b]	0.7								
			Lws in Ph-rich domain (ECL)	8.5	1.5	7.8	0.8	9.4	0.8						
	17RB-3C	Interlayered BLS/ECL	Lws in Grt (BLS)	9.3	1.4	8.2	0.8	10.4	0.8	8.4[a]	0.4	9.6[a]	0.8		
			Matrix Lws (BLS)	9.0	1.4	8.0	0.8	9.4	0.8						
			Matrix Grt (BLS)	8.1	1.3	6.9	0.6	9.5	0.6	6.9	0.6	8.3	0.6		
Rio San Juan, Dominican Republic	IEC15–3.5	BLS-facies metagabbro	Matrix Lws	7.9	0.3	7.6	0.5	8.0	0.5	7.9[a]	0.2	7.7	0.4		
South Motagua, Guatemala	MVE04-7-2	ECL	Matrix Lws	10.3	2.0	8.3	0.7	11.7	0.7						
			Matrix Grt	9.6	1.3	7.6	0.6	10.8	0.6	9.7[a]	0.9	8.4	0.6		
	01GSn2-9	Omphacitite	Matrix Lws	9.5	1.5	8.7	0.7	11.0	0.7						
Ring Mt., Franciscan Complex	LVT-1	Interlayered BLS/ECL	Matrix Lws (ECL)	8.4	1.6	7.5	0.4	9.5	0.3						
			Lws-vein (ECL)	8.0	0.6	7.6	0.3	8.5	0.3	8.0	0.3	7.8[a]	0.7		
			Lws in Grt (BLS)	7.6	0.2	7.5	0.3	7.7	0.3						
			Matrix Lws (BLS)	8.6	0.3	8.5	0.3	8.8	0.3	8.5[a]	0.1	8.8	0.3		
			Lws-vein (BLS)	8.5	0.4	8.1	0.4	8.7	0.3	8.7[a]	0.2	8.4[a]	0.5		
	RR-1	BLS	Matrix Lws	9.3	0.4	8.9	0.3	9.6	0.3	9.5	0.3	9.1	0.3		
			Lws in Cal-vein	10.2	0.6	9.7	0.3	10.5	0.3	10.3[a]	0.4	10.1[a]	0.6		
N Berkeley Hills, Franciscan Complex	EC-1B	BLS	Matrix Lws	9.6	0.5	9.1	0.3	9.9	0.3	9.7	0.3	9.7	0.3		
			Lws-vein	9.2	1.5	8.0	0.7	10.6	0.7			8.6[a]	1.1		
			Lws-vein, replaced by Chl + Pmp	8.9	1.6	6.6	0.2	10.3	0.2			9.7[a]	1.0		
Siliciclastic-matrix mélange															
Blind Beach, Franciscan Complex	SM-8	BLS	Matrix Lws	9.4	0.5	9.0	0.5	9.7	0.5			9.2	0.5		
Structurally coherent terrane															
Catalina Schist, Santa Catalina Island	B16-11	BLS	Matrix Lws	11.9	1.2	10.8	0.9	12.9	0.9						
	B16-006	Grt-bearing BLS	Matrix Lws	11.8	1.4	10.4	0.9	13.2	0.9						
Diahot terrane, New Caledonia	NC19-159	BLS-facies metagabbro	Matrix Lws	6.4	1.8	4.9	0.7	7.7	0.6	6.1[a]	1.5	6.7[a]	1.9		
Alpine Corsica, France	C13	Lws-Omp metagabbro	Matrix Lws	4.0	0.4	3.7	0.5	4.3	0.5	4.1	0.4	4.0[a]	0.4		
	COR18-PK3	Metasomatite (Lws ~25%)	Matrix Lws	11.5	1.9	10.2	0.4	13.3	0.4						
	COR18-PK4	Metasomatite (Lws >75%)	Matrix Lws	12.2	1.5	10.7	0.4	13.4	0.4						
			Lws in Qz-vein	11.0	2.0	9.7	0.4	12.5	0.4						
Sivrihisar Massif, Turkey	SV08-283C	ECL	Matrix Lws	12.9	0.3	12.7	0.5	13.1	0.5	12.8[a]	0.1	13.0[a]	0.0		
			Matrix Grt	12.1	1.1	11.1	0.7	12.9	0.7	12.4	0.7	11.1	0.7	11.9[a]	0.9

10.1029/2023GC011389

Table 2
Continued

Location	Sample	Rock type	Texture	Avg $\delta^{18}O$	2σ	Min $\delta^{18}O$	2σ	Max $\delta^{18}O$	2σ	Core $\delta^{18}O$	2σ	Rim $\delta^{18}O$	2σ	Outermost rim $\delta^{18}O$	2σ
	SV01-75A	BLS	Matrix Lws	14.1	1.0	12.8	0.4	14.8	0.4	14.2	0.4	14.3	0.5		
			Matrix Grt	20.7	1.1	20.1	0.7	21.9	0.7	21.8	0.7	20.4[a]	0.6		
	SV01-50A	Interlayered BLS/ECL	Matrix Lws (ECL)	11.8	0.3	11.7	0.5	12.0	0.4	11.8	0.5	11.7[a]	0.2		
			Lws in Cal-vein (ECL)	11.7	0.4	11.5	0.4	12.1	0.5	11.6[a]	0.0	12.0[a]	0.5		
			Matrix Lws (BLS)	12.1	0.3	12.0	0.5	12.4	0.5	12.1[a]	0.5	12.2[a]	0.3		
			Lws in Cal-vein (BLS)	12.2	0.2	12.0	0.5	12.4	0.5	12.2	0.5	12.3[a]	0.1		
	TZ10-2.2C	Metasomatite	Matrix Lws	14.1	0.5	13.6	0.5	14.7	0.5	13.8[a]	0.5	14.0[a]	0.4		
	SV08-281D	Quartzite	Matrix Lws	20.6	1.4	19.9	0.6	22.1	0.5						
			Matrix Grt1	23.2	0.7	22.7	0.6	23.5	0.6	23.5	0.6	22.7	0.6		
			Matrix Grt2	22.7	1.7	21.9	0.6	23.6	0.6	23.6	0.6	22.5	0.6	21.9	0.6
	SV08-7ADD	Calcschist	Matrix Lws	24.1	1.3	22.7	0.5	24.9	0.5						
Boulders															
Pinchi Lake, British Columbia	BLR5	ECL	Matrix Lws	14.6	0.5	14.1	0.3	14.9	0.3	14.4[a]	0.4	14.6[a]	0.7		
			Lws in Ph-vein	14.8	1.1	13.8	0.3	15.1	0.3	15.0[a]	0.0				
			Matrix Grt	13.1	0.5	12.7	0.5	13.7	0.5	13.1[a]	0.4	13.0[a]	0.1		
	BLR4	Retrogressed ECL	Lws in Grt	14.3	1.1	13.7	0.3	15.1	0.3						
			Matrix Lws	14.2	1.1	13.4	0.3	15.2	0.3	14.4[a]	0.6	14.0[a]	1.0		
Xenolith															
Garnet Ridge, Colorado Plateau	17GR11	ECL-facies xenolith	Matrix Lws	10.2	1.0	9.6	0.8	11.0	0.8						
			Matrix Grt	9.1	1.5	7.8	0.6	10.2	0.6	9.5[a]	0.7	7.8[a]	0.0		

[a]Average oxygen isotope composition at the core and rim of lawsonite or garnet. [b]Single point analysis.

Geochemistry, Geophysics, Geosystems

10.1029/2023GC011389

Table 3
Garnet Major and Minor Element Compositions

	Serpentinite-matrix mélange					Structurally coherent terrane											Boulder		Xenolith	
	Rocky Beach, Port Macquarie		South Motagua, Guatemala			Sivrihisar Massif, Turkey											Pinchi Lake, British Columbia		Garnet Ridge, Colorado Plateau	
Location	17RB-3C GRT BLS		MVE04-7-2 ECL			SV08-283C ECL			SV01-75A BLS		SV08-281D Grt1 (quartzite)			SV08-281D Grt2 (quartzite)			BLR5 (ECL)		17ER11-GR (xenolith)	
Sample	Core	Mn-poor rim	Core	Mn-rich peak	Rim	Core	Rim	Outermost rim	Core	Rim	Core	Rim	Outermost rim	Core	Rim	Outermost rim	Core	Rim	Core	Rim
SiO_2	37.4	37.4	37.2	37.4	37.9	37.4	37.5	37.7	36.9	37.4	37.1	36.7	37.1	37.2	37.2	36.4	36.8	37.6	38.1	39.7
TiO_2	0.23	0.09	0.15	0.10	0.05	0.07	0.14	0.11	0.05	0.72	0.10	1.22	0.08	0.06	0.09	0.15	0.16	0.04	0.11	b.d.l.
Al_2O_3	20.3	20.5	20.4	20.7	21.0	20.5	20.7	20.5	20.3	20.7	20.2	20.0	20.3	20.6	20.9	20.1	20.4	21.2	20.2	21.3
Cr_2O_3	b.d.l.	b.d.l.	0.12	b.d.l.	b.d.l.	b.d.l.	b.d.l.	0.05	b.d.l.	b.d.l.	b.d.l.	b.d.l.	0.05	b.d.l.	b.d.l.	b.d.l.	b.d.l.	b.d.l.	0.05	0.04
FeO_T	28.3	29.3	31.3	30.7	30.6	24.4	25.9	26.7	23.7	27.6	1.21	1.06	1.01	1.14	1.13	3.28	27.4	29.8	26.3	26.3
MnO	1.47	0.35	0.88	1.17	0.73	5.52	2.74	3.00	6.80	3.40	35.6	34.8	34.8	35.0	35.0	31.5	5.68	0.64	3.83	0.86
MgO	1.21	1.85	2.06	2.19	2.60	2.22	2.20	1.80	1.09	1.65	1.67	1.92	2.00	1.78	1.90	1.56	1.15	2.75	4.31	6.52
CaO	10.8	10.0	7.90	8.15	7.86	9.18	10.1	9.56	10.2	8.48	4.08	4.17	4.25	4.36	4.36	5.99	7.12	7.23	6.52	5.10
Na_2O	b.d.l.	0.02	b.d.l.	b.d.l.	b.d.l.	b.d.l.	b.d.l.	0.02	b.d.l.	b.d.l.	0.03	0.02	0.02	0.03	0.05	b.d.l.	0.02	b.d.l.	b.d.l.	0.02
K_2O	b.d.l.	b.d.l.	b.d.l.	b.d.l.	b.d.l.	b.d.l.	b.d.l.	0.03	b.d.l.	b.d.l.	b.d.l.	b.d.l.	b.d.l.	b.d.l.	0.02	0.03	b.d.l.	b.d.l.	b.d.l.	b.d.l.
TOTAL	99.8	99.6	100.0	100.4	100.7	99.3	99.3	99.4	99.0	99.9	99.9	100.0	99.6	100.2	100.7	99.0	98.8	99.2	99.5	99.9
Normalized to 12 oxygens and 8 Cations																				
Si	3.00	2.99	2.98	2.97	3.00	3.00	3.00	3.02	2.98	2.99	3.00	2.97	3.00	2.99	2.98	2.96	3.00	3.01	3.03	3.09
Ti	0.01	0.01	0.01	0.01	0.00	0.00	0.01	0.01	0.00	0.04	0.01	0.07	0.01	0.00	0.01	0.01	0.01	0.00	0.01	0.00
Al	1.92	1.93	1.92	1.94	1.95	1.94	1.95	1.93	1.93	1.95	1.92	1.91	1.93	1.96	1.96	1.92	1.96	2.00	1.89	1.96
Cr	0.00	0.00	0.01	0.00	0.00	0.00	0.00	0.00	0.00	0.00	0.00	0.00	0.00	0.00	0.00	0.00	0.00	0.00	0.00	0.00
Fe^{2+}	1.84	1.89	2.01	1.95	1.98	1.57	1.69	1.78	1.51	1.85	0.01	0.06	0.00	0.02	0.00	0.08	1.85	2.00	1.71	1.71
Fe^{3+}	0.06	0.07	0.09	0.10	0.04	0.06	0.04	0.01	0.10	0.00	0.08	0.01	0.07	0.06	0.08	0.14	0.01	0.00	0.04	0.00
Mn	0.10	0.02	0.06	0.08	0.05	0.37	0.19	0.20	0.47	0.23	2.43	2.38	2.38	2.38	2.37	2.17	0.39	0.04	0.26	0.06
Mg	0.14	0.22	0.25	0.26	0.31	0.27	0.26	0.21	0.13	0.20	0.20	0.23	0.24	0.21	0.23	0.19	0.14	0.33	0.51	0.76
Ca	0.93	0.86	0.68	0.70	0.67	0.79	0.87	0.82	0.88	0.73	0.35	0.36	0.37	0.38	0.37	0.52	0.62	0.62	0.55	0.42
Na	0.00	0.00	0.00	0.00	0.00	0.00	0.00	0.00	0.00	0.00	0.00	0.00	0.00	0.00	0.01	0.00	0.00	0.00	0.00	0.00
K	0.00	0.00	0.00	0.00	0.00	0.00	0.00	0.00	0.00	0.00	0.00	0.00	0.00	0.00	0.00	0.00	0.00	0.00	0.00	0.00
Pyrope	0.05	0.07	0.08	0.09	0.10	0.09	0.09	0.07	0.04	0.07	0.07	0.08	0.08	0.07	0.08	0.06	0.05	0.11	0.17	0.26

Geochemistry, Geophysics, Geosystems

10.1029/2023GC011389

Table 3
Continued

	Serpentinite-matrix mélange					Structurally coherent terrane											Boulder		Xenolith	
	Rocky Beach, Port Macquarie		South Motagua, Guatemala			Sivrihisar Massif, Turkey											Pinchi Lake, British Columbia		Garnet Ridge, Colorado Plateau	
Location	17RB-3C GRT BLS		MVE04-7-2 ECL			SV08-283C ECL			SV01-75A BLS		SV08-281D Grt1 (quartzite)			SV08-281D Grt2 (quartzite)			BLR5 (ECL)		17ER11-GR (xenolith)	
Sample	Core	Mn-poor rim	Core	Mn-rich peak	Rim	Core	Rim	Outermost rim	Core	Rim	Core	Rim	Outermost rim	Core	Rim	Outermost rim	Core	Rim	Core	Rim
Grossular	0.27	0.25	0.17	0.18	0.20	0.23	0.26	0.26	0.25	0.22	0.08	0.08	0.09	0.09	0.08	0.10	0.19	0.21	0.16	0.14
Almandine	0.61	0.63	0.67	0.65	0.66	0.52	0.56	0.59	0.50	0.62	0.00	0.02	0.00	0.01	0.00	0.03	0.62	0.67	0.56	0.58
Andradite	0.03	0.04	0.04	0.05	0.02	0.03	0.02	0.01	0.05	0.00	0.04	0.00	0.03	0.03	0.04	0.07	0.01	0.00	0.02	0.00
Spessertine	0.03	0.01	0.02	0.03	0.02	0.12	0.06	0.07	0.16	0.08	0.81	0.78	0.80	0.80	0.80	0.73	0.13	0.01	0.08	0.02

Note. FeO* = all iron reported as FeO wt%; b.d.l. = less than detection limit.

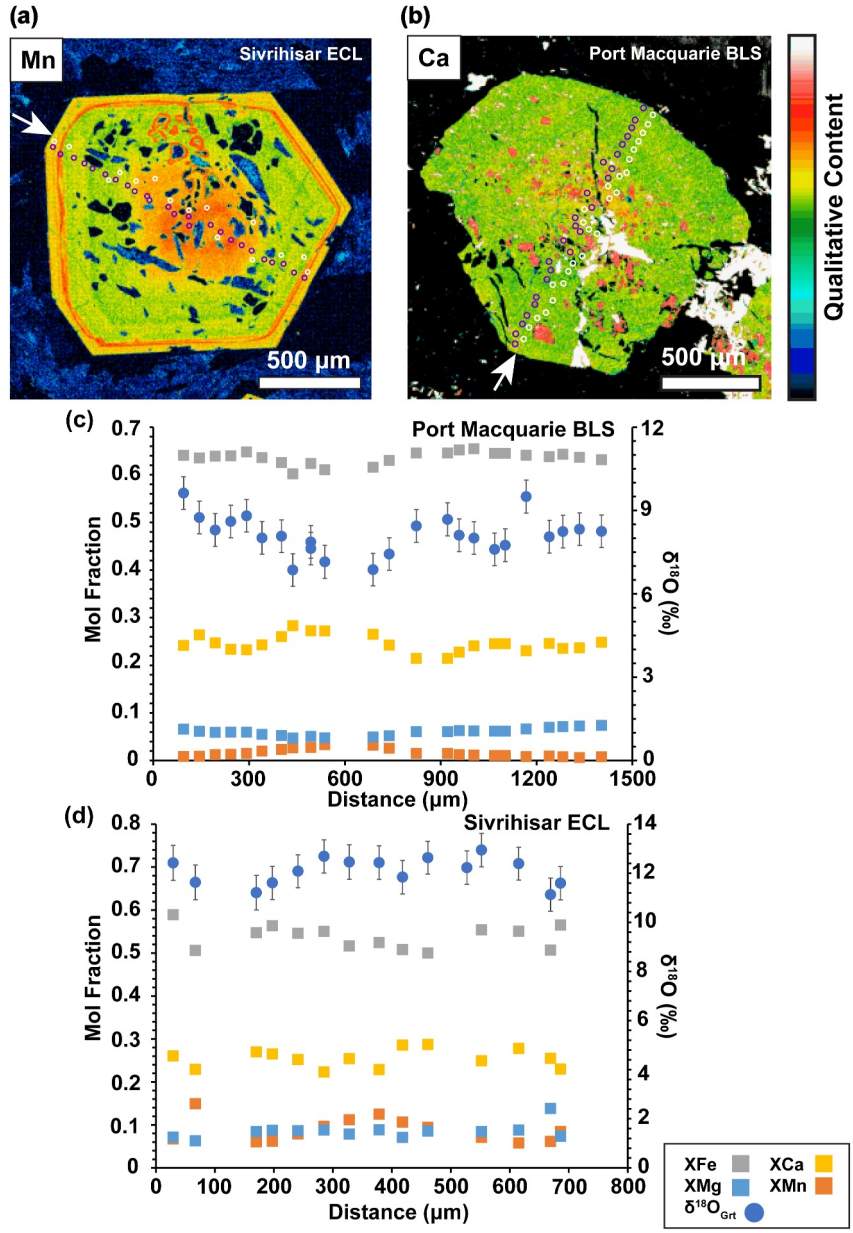

Figure 5. (a, b) Element zoning in garnet from Sivirihisar eclogite (SV08-283C; a) and the blueschist layer of Port Macquarie interlayered blueschist/eclogite (17RB-3C; b). (c, d) Major/minor element composition and $\delta^{18}O$ zoning profiles of garnet from the Port Macquarie blueschist layer (17RB-3C; c) and the Sivrihisar eclogite (SV08-283C; d). White arrows indicate the starting positions of analytical traverses. Purple dots = point analysis locations of major/minor element composition; White dots = point analysis locations of $\delta^{18}O$; Error bar of $\delta^{18}O_{Grt} = \pm 2\sigma$.

interlayered blueschist/eclogite 17RB-3C: 1.4‰) toward the rims (Figure 4 and Table 2). Each oscillatory-zoned garnet reveals distinct correlations between its $\delta^{18}O$ and major/minor element concentrations: Port Macquarie $\delta^{18}O_{Grt}$, positively correlated with Mg and Fe but negatively correlated with Ca and Mn (Figure 5c); S. Motagua FZ $\delta^{18}O_{Grt}$, positively correlated with Mn; and Garnet Ridge $\delta^{18}O_{Grt}$, negatively correlated with Ca. Garnet in the Pinchi Lake eclogite (BLR5) preserves <1‰ variations.

5. Modeling Methods and Results

In this section, we describe modeling methods and results used to investigate the major controls on garnet and lawsonite oxygen isotope composition and variations.

Table 4
Time Interval of Garnet Growth Determined From the Ages of Lawsonite-Bearing HP/LT Rocks

Location	Rock type	Interpretation	Age (Ma)	Isotopic system	Growth interval (Ma)
Rocky Beach, Port Macquarie	ECL	prograde age	489.7 ± 5.5–487.0 ± 11	Lu-Hf[a]	8.4–25
	BLS	peak-to-cooling age	472.4 ± 1.7–464 ± 3.9	Sm-Nd[a]	
South Motagua, Guatemala	ECL		140–120	Sm-Nd[b]	20
Sivrihisar Massif, Turkey	Lws ECL	prograde age	93.0 ± 1.8–91.1 ± 1.3	Lu-Hf[c]; $^{40}Ar/^{39}Ar$[d]	9.3–11.2
	Ep ECL	cooling age	81.8 ± 2.2	$^{40}Ar/^{39}Ar$[d]	
Garnet Ridge, Colorado Plateau	Xenolith	prograde-to-cooling age	81–35	U-Pb[e,f]	46

[a]Tamblyn, Hand, Kelsey, et al. (2020). [b]Brueckner et al. (2009). [c]Mulcahy et al. (2014). [d]Fornash et al. (2016). [e]Usui et al. (2003). [f]Smith et al. (2004).

5.1. Diffusion Profiles of $\delta^{18}O_{Grt}$

To evaluate the effect of intracrystalline diffusion on $\delta^{18}O_{Grt}$, the diffusion profile of $\delta^{18}O_{Grt}$ was calculated as a function of time at the peak condition for 4 selected garnet + lawsonite-bearing samples (3 eclogites (SV08-283C, MVE04-7-2, 17GR11), and 1 blueschist (17RB-3C)). The length scale of $\delta^{18}O_{Grt}$ variation is not negligible relative to the diameter of each garnet analyzed (Figure 5). Therefore, spherical geometry was considered to model the diffusion profile, in which the oxygen isotope composition at a radial distance (r; a distance from garnet core) is expressed as (Crank, 1979):

$$C(r,t) = C_1 + \frac{1}{2}(C_0 - C_1)\left[\mathrm{erf}\left(\frac{a+r}{2\sqrt{Dt}}\right) + \mathrm{erf}\left(\frac{a-r}{2\sqrt{Dt}}\right)\right] - \frac{(C_0 - C_1)}{r}\sqrt{\frac{Dt}{\pi}}\left[\exp\left(\frac{-(a-r)^2}{4Dt}\right) - \exp\left(\frac{-(a+r)^2}{4Dt}\right)\right] \quad (1)$$

C_0 and C_1 are $\delta^{18}O$ at garnet core and rim, a is the radius of garnet, t is the timescale of garnet growth, and D (m^2/s) is a diffusion coefficient. This study used a diffusion coefficient associated with fast diffusion pathways (i.e., interstitial sites) (Scicchitano et al., 2022) to maximize the influence of intracrystalline diffusion in modeling $\delta^{18}O_{Grt}$ variations. The longest time interval for garnet growth was determined based on the published prograde-to-peak metamorphic ages (Table 4). For comparison, additional diffusion profiles were constructed using an arbitrary long time interval of 10 Ga to assess the influence of growth time interval on $\delta^{18}O_{Grt}$ variations.

5.2. Water-Rock Ratio and Metasomatic Fluid $\delta^{18}O$

This study used Monte Carlo simulations to investigate potential correlations between water-rock ratio (W/R) and the $\delta^{18}O$ of fluid that led to the formation of lawsonite-bearing Tavşanlı (TZ10-2.2C) and Corsica metasomatites (COR18-PK3, PK4). All targeted metasomatites formed along lithological contacts but at the expense of different lithologies. The Tavşanlı metasomatite likely formed at the expense of serpentinite lenses that have an ultramafic protolith (Kang et al., 2022), whereas the Corsica metasomatites preferentially form within carbonaceous metapelites (Martin et al., 2011; Vitale Brovarone et al., 2014, 2020). Major parameters that control lawsonite $\delta^{18}O$ in these metasomatites include (a) the $\delta^{18}O$ of fluid, (b) the temperature, and (c) the W/R at the time of fluid-rock interactions. $\delta^{18}O_{Water}$ during lawsonite growth can be expressed in terms of the last two variables as well as $\delta^{18}O_{Lws}$ by applying a mass-balance equation as follows:

$$\delta^{18}O_{Water} = \frac{\left(\delta^{18}O_{Lws-bearing\ metasomatite} - \delta^{18}O_{Precursor\ rock}\right) + W/R\left(\delta^{18}O_{Lws} - 1000\ln\alpha_{Lws-Water}\right)}{W/R} \quad (2)$$

where $\delta^{18}O_{Water}$, $\delta^{18}O_{Lws\text{-}bearing\ metasomatite}$, $\delta^{18}O_{Precursor\ rock}$, and $\delta^{18}O_{Lws}$ are the oxygen isotope compositions of fluid, lawsonite-bearing metasomatite, precursor rock of metasomatite, and lawsonite, respectively. One million simulations were run to calculate $\delta^{18}O_{Water}$ in $300 \le T\ (°C) \le 800$ and $0 \le W/R \le 1{,}000$. $\delta^{18}O_{Precursor\ rock}$ was constrained based on the $\delta^{18}O$ of potential precursor rock of each sample (peridotite for Tavşanlı metasomatite: 5.3–5.7‰; calcschist for Corsica metasomatites: 20–35‰) (Eiler, 2001; Kang et al., 2022; Vitale Brovarone

Table 5
Measured and Calculated Bulk $\delta^{18}O$ of Lawsonite-Bearing Metasomatite

Location	Sample	Rock type	Bulk $\delta^{18}O$ (‰)
Alpine Corsica, France	COR18-PK3	Metasomatite (Lws > 75 vol%)	4.7–10.4
	COR18-PK4	Metasomatite (Lws ~ 25 vol%)	4.4–5.5
Sivrihisar Massif, Turkey	TZ10-2.2C	Metasomatite	12.2

et al., 2014). $\delta^{18}O_{\text{Lws-bearing metasomatite}}$ of each sample was previously measured or estimated from the modes and oxygen isotope compositions of matrix minerals (Table 5) (Gauthiez Putallaz, 2017; Martin, Rubatto, et al., 2014).

5.3. Modeling Results

5.3.1. Diffusion Profiles of $\delta^{18}O_{Grt}$

The $\delta^{18}O_{Grt}$ gradient of modeled diffusion profile becomes smoother at 10 Ga compared to the maximum growth interval estimated from prograde-to-peak metamorphic ages (Figure 6). However, none of the modeled $\delta^{18}O_{Grt}$ diffusion profiles reproduce the measured $\delta^{18}O_{Grt}$ variations (Figure 6). In the Sivrihisar eclogite (SV08-283C), the modeling results of $\delta^{18}O_{Grt}$ diffusion profiles increasingly deviate from the measured $\delta^{18}O_{Grt}$ from the core to the rims (Figure 6a). The measured $\delta^{18}O_{Grt}$ gradually falls below the profile, with a difference of up to 1.7‰ at the rims (Figure 6a). However, the gap between the measured and modeled $\delta^{18}O_{Grt}$ decreases toward the oscillatory-zoned outermost rims (Figure 6a).

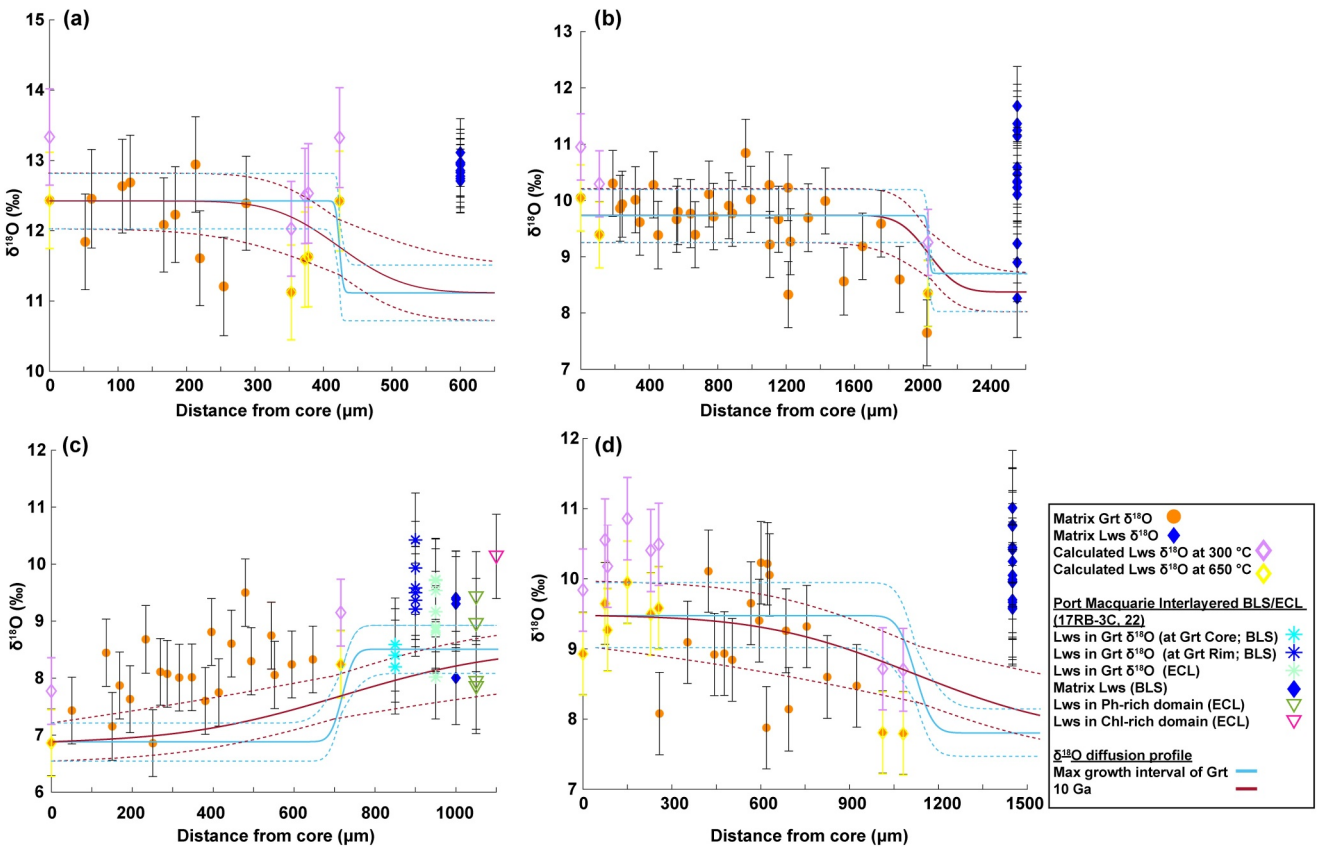

Figure 6. Modeled $\delta^{18}O$ diffusion profiles of garnet in Sivrihisar eclogite (a; SV08-283C), South Motagua eclogite (b; MVE04-7-2), Port Macquarie interlayered blueschist/eclogite (c; 17RB-3C), and eclogite-facies Garnet Ridge xenolith (d; 17GR11). Uncertainties (dotted lines) were propagated from 2σ uncertainties on diffusion coefficient (Scicchitano et al., 2022) and measured $\delta^{18}O_{Grt}$. Note measured $\delta^{18}O_{Lws}$ was plotted at an arbitrary position, but calculated $\delta^{18}O_{Lws}$ was plotted along with the corresponding $\delta^{18}O_{Grt}$ at the relevant radial distance in each plot.

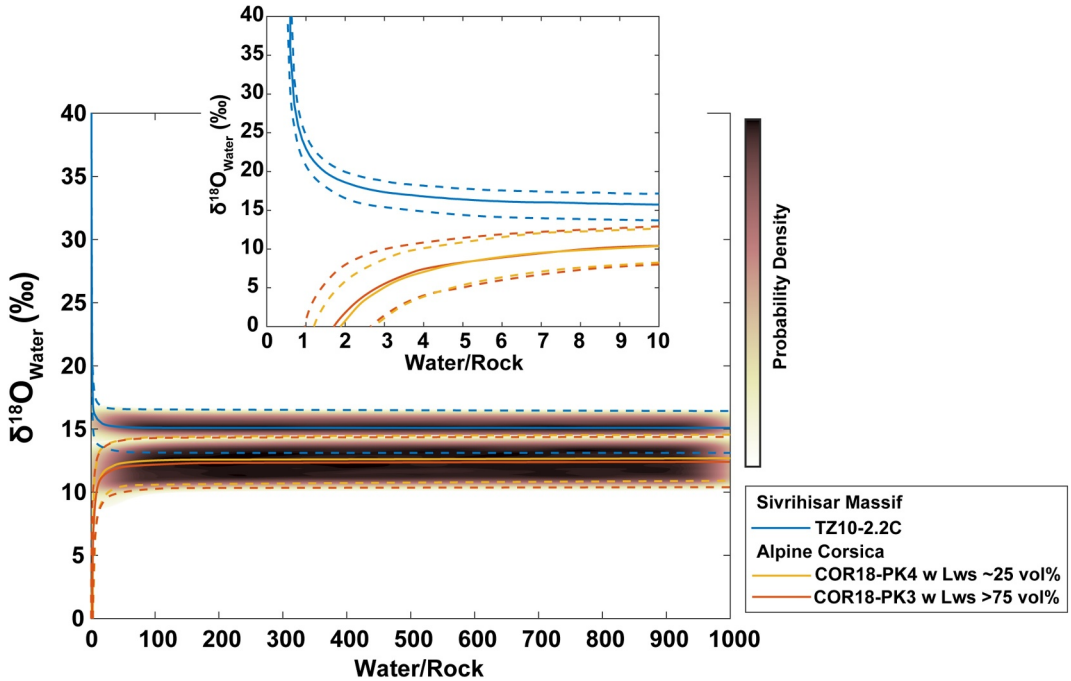

Figure 7. Results of Monte Carlo simulations, showing a relationship between $\delta^{18}O_{Water}$ and *W/R*. Inset of this figure is a magnified image of the original diagram at $0 \leq W/R \leq 1$. Solid lines = average $\delta^{18}O_{Water}$ of the simulated results; Dashed lines = minimum and maximum $\delta^{18}O_{Water}$ of the simulated results; The color bar = probability density.

The $\delta^{18}O_{Grt}$ diffusion profiles of oscillatory-zoned garnets either show a gradual decrease or increase in $\delta^{18}O$ (Figures 6b–6d). Despite the variations in overall patterns, they show a similar extent of deviation from the measured $\delta^{18}O_{Grt}$ toward the rims in the S. Motagua FZ eclogite (MVE04-7-2: up to −2.2‰), the blueschist layer of the Port Macquarie interlayered blueschist/eclogite (17RB-3C: up to 3‰), and the Garnet Ridge xenolith (17GR11: up to −2.1‰) (Figures 6b–6d).

5.3.2. Water-Rock Ratio and Metasomatic Fluid $\delta^{18}O$

The result of simulations shows that the metasomatic fluid predicted from the Tavşanlı metasomatite (TZ10-2.2C) is ≥13.1‰ across the entire range of $0 \leq W/R \leq 1{,}000$ (Figure 7). However, $\delta^{18}O_{Water}$ converges to 15.1 ± 2.0‰ with increasing *W/R* but increases significantly at $W/R \leq 1$ (Figure 7). In contrast, two Corsica metasomatites (COR18-PK3, 4) predict metasomatic fluids with $\delta^{18}O_{Water} \leq 14.4$‰ (Figure 7). Regardless of different lawsonite modes, the $\delta^{18}O_{Water}$ of Corsica metasomatites converges to similar values (COR18-PK4 with ~25% of lawsonite: 12.7 ± 1.8‰; COR18-PK3 with >75% of lawsonite: 12.4 ± 2.1‰) (Figure 7). The *W/R* corresponding to the Corsica $\delta^{18}O_{Water}$ is consistently predicted to be ≥1 (Figure 7). In all cases of Tavşanlı and Corsica metasomatites, the simulated probability tends to increase as the $\delta^{18}O_{Water}$ of each metasomatite approaches its converging value (Figure 7), with the maximum probability density at $W/R > 1$ (TZ10-2.2C: 622; COR18-PK4: 416; COR18-PK3: 316).

6. Discussion

The main factors that may influence the oxygen isotope composition of lawsonite are temperature (Taylor & Coleman, 1968; Vho et al., 2019), isotopic fractionation with coexisting minerals and/or infiltrating fluids (e.g., Gauthiez Putallaz, 2017; Martin, Rubatto, et al., 2014; Taylor & Coleman, 1968; Vho et al., 2019, 2020), water/rock ratio (e.g., Vho et al., 2020), and intracrystalline diffusivity during the growth of lawsonite. The following sections investigate the potential influence of each factor on $\delta^{18}O_{Lws}$ in order to distinguish fluid-related variations in $\delta^{18}O_{Lws}$.

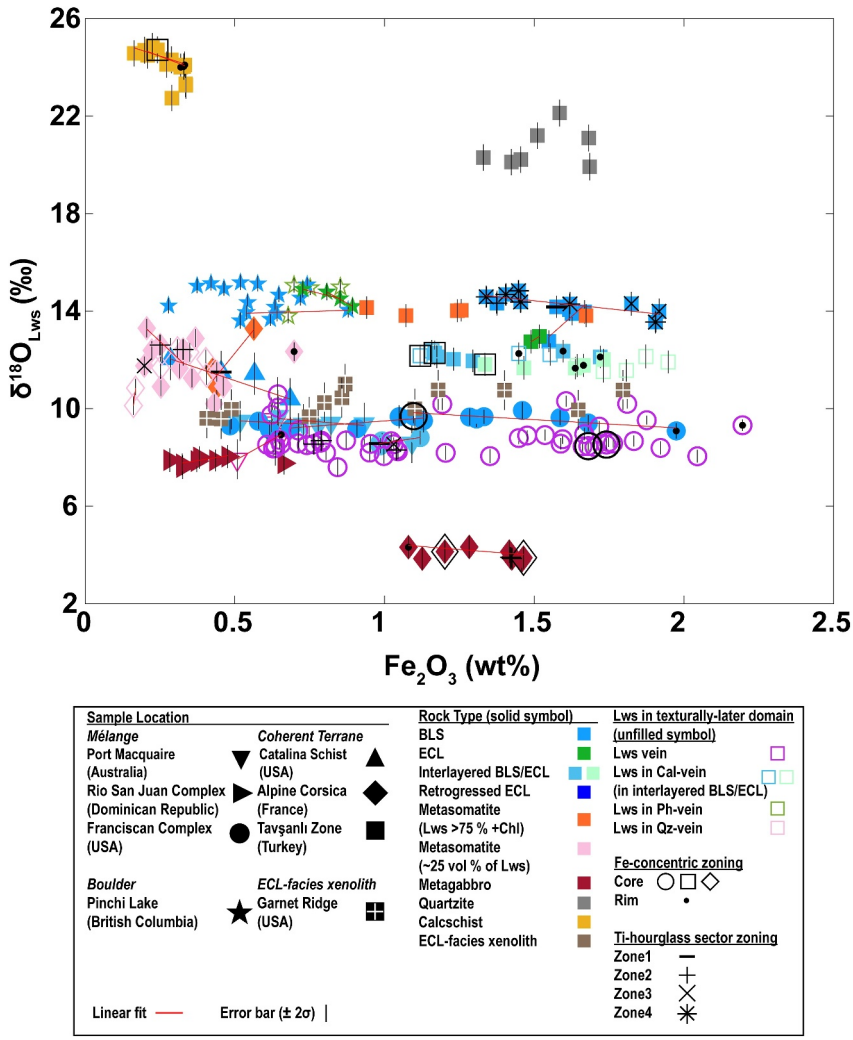

Figure 8. $\delta^{18}O$ versus Fe_2O_3 in lawsonite from selected blueschist- to eclogite-facies 12 metabasalts (Port Macquarie 17RB-22, 3C, Ring Mt. LVT-1, RR-1, N. Berkeley Hills EC-1B, Blind Beach SM-8, Catalina B16-006, Sivrihisar SV08-283C, SV01-75A, 50A, and Pinchi Lake BLR4, 5), 1 eclogite-facies xenolith (17GR11), 2 metagabbros (Rio San Juan IEC15–3.5, Corsica C13), 3 metasomatites (Corsica COR18-PK3, 4, Tavşanlı TZ10-2.2C), and 2 metasediments (Sivrihisar SV08-281D, 7ADD). Filled symbols indicate matrix lawsonite, and unfilled symbols indicate lawsonite in texturally later domains (e.g., vein). Symbols other than black horizontal lines, dots, crosses, "*x*" symbols, and asterisks represent different subduction complexes, with different colors indicating different lithologies of lawsonite-bearing host rocks or different texturally later lawsonite-bearing domains. Fe_2O_3 concentrations of lawsonite were partially obtained from Kang et al. (2022).

6.1. Correlations Between $\delta^{18}O_{Lws}$ and Lawsonite Major/Minor Element Composition

Analyzed lawsonite grains show a wide range of major and minor element compositions, with weight percent concentrations of Fe, Ti, and/or Cr (Table 1). To evaluate the potential effect of lawsonite composition on the analytical bias of $\delta^{18}O_{Lws}$ (i.e., matrix-bias), systematic correlations were investigated between element concentrations and $\delta^{18}O_{Lws}$, using weighted linear regression that accounts for the uncertainty of $\delta^{18}O_{Lws}$. Fe_2O_3*, TiO_2, Al_2O_3, CaO, Cr_2O_3, Fe_2O_3* + TiO_2, and Cr_2O_3 + TiO_2 do not vary systematically with $\delta^{18}O_{Lws}$, but instead show different correlations (i.e., positively, negatively, or non-correlated) from individual grain to grain (Figure 8). The lack of a systematic relationship supports a negligible matrix effect on the measurement of $\delta^{18}O_{Lws}$, which is consistent with the previous estimate of a minor $\delta^{18}O_{Lws}$ bias (−0.3‰) with varying Fe_2O_3* ± TiO_2 content (Melnik et al., 2023). Therefore, any noticeable variations in $\delta^{18}O_{Lws}$ (at least >0.3‰) as well as correlations with major/minor element concentrations likely stem from factors other than matrix effect.

6.2. Temperature Effect on Isotopic Fractionation Between $\delta^{18}O_{Lws}$, $\delta^{18}O_{Grt}$, and $\delta^{18}O_{Water}$

Lawsonite undergoes changes in its oxygen isotope composition as it experiences isotopic fractionation with coexisting minerals (e.g., garnet) and/or fluid during its growth. The extent of isotopic fractionation between lawsonite and coexisting phases (minerals, fluids) is a function of the temperature at which they are isotopically equilibrated.

An oxygen isotope fractionation factor between lawsonite and aqueous fluid can be derived from a fractionation factor between lawsonite and quartz and between water and quartz using the following relation:

$$\delta^{18}O_{Lws} - \delta^{18}O_{Water} \approx 1000\ln\alpha_{Lws-Water} = 1000\ln\alpha_{Lws-Qz} - 1000\ln\alpha_{Water-Qz}$$

$$= (A_{Lws-Qz} - A_{Water-Qz}) * \frac{10^6}{T^2} + (B_{Lws-Qz} - B_{Water-Qz}) * \frac{10^3}{T} + (C_{Lws-Qz} - C_{Water-Qz}) \quad (3)$$

A, B, and C are polynomial parameters associated with each of these fractionation factors (Vho et al., 2019). This approximation is valid when the temperature is sufficiently high (>200°C) to ensure that oxygen isotope fractionation between two phases is <~10‰ (Sharp, 2007). Lawsonite-bearing HP/LT rocks, including the samples analyzed in this study, typically record peak conditions of 300–650°C, which satisfies this condition (e.g., Davis & Whitney, 2006; Vitale Brovarone et al., 2011; see Tables 1 and 2 in Whitney et al. (2020)).

Similarly, the oxygen isotope fractionation factor between garnet and lawsonite at $T > 200$°C can be described as follows:

$$1000\ln\alpha_{Grt-Lws} = 1000\ln\alpha_{Grt-Qz} - 1000\ln\alpha_{Lws-Qz} \quad (4)$$

where 1,000 $\ln\alpha_{Grt\text{-}Qz}$ is approximated as a linear combination of fractionations between each garnet end-member and quartz, since garnet is a solid solution consisting of multiple end-members (Kohn, 1993; Vho et al., 2019):

$$1000\ln\alpha_{Grt-Qz} \approx \sum\left(A_{i-Qz} * \frac{10^6}{T^2} + B_{i-Qz} * \frac{10^3}{T} + C_{i-Qz}\right) * X_i * \frac{N_i}{N_{Grt}} \quad (5)$$

X_i is the molar fraction of end-member i in garnet, N_i is the number of moles of oxygen in end member i, and N_{Grt} is the number of moles of oxygen in garnet. A_{i-Qz}, B_{i-Qz}, and C_{i-Qz} are polynomial parameters that define the fractionation between each garnet end-member i and quartz (Vho et al., 2019). The amount of oxygen isotope fractionation was assessed for the lawsonite–water and garnet–lawsonite pairs within the range of 300–650°C. The molar fraction of each garnet end-member (X_i) was randomly generated (5 million different numbers) and applied in Equation 5 at 300–650°C, while ensuring that the sum of all X_i values was equal to unity.

Our results indicate that $\delta^{18}O_{Water}$ is positively correlated with $\delta^{18}O_{Lws}$ (Figure 9a). $\delta^{18}O_{Water}$ differs by 0.2–1.3‰ from $\delta^{18}O_{Lws}$ at 650 to 300°C (Figure 9a). For a given $\delta^{18}O_{Water}$, $\delta^{18}O_{Lws}$ increases by ~1.7‰ as T decreases from 650 to 300°C (Figure 9a). $\delta^{18}O_{Grt}$ varies up to 0.9‰ at 300–650°C, and its difference from $\delta^{18}O_{Lws}$ changes from −0.9 to 0.02‰ as temperature increases from 300 to 650°C (Figure 9b). $\delta^{18}O_{Grt}$ becomes lighter than $\delta^{18}O_{Water}$ by −0.5‰ to −1.4‰ with increasing temperature from 300 to 650°C (Figure 9c). If $\delta^{18}O$ fractionation between garnet and water is estimated with the actual X_i values of garnet compositions (not randomly generated) and different polynomial parameters (Zheng, 1993), the corresponding maximum $\delta^{18}O_{Grt}$ variation at 300–650°C is 0.7‰, which only differs by −0.2‰ from the simulation result. Therefore, if lawsonite, garnet, and fluid were in isotopic equilibrium, temperature variations within 300–650°C wouldn't result in $\delta^{18}O$ variations that exceed ~1.7‰ in lawsonite and ~0.9‰ in garnet.

6.3. Diffusion Profiles of $\delta^{18}O_{Grt}$: Implications for Fluid-Rock Interactions and Diffusion of $\delta^{18}O_{Lws}$

The modeling results of $\delta^{18}O_{Grt}$ diffusion profiles vary among different samples, but none of the measured $\delta^{18}O_{Grt}$ variations can be modeled solely by intracrystalline diffusion within a reasonable timescale (Figure 6). In the Sivrihisar eclogite (SV08-283C), garnet deviates by up to −1.7‰ at the rims and positively deviates toward the oscillatory-zoned outermost rims (Figure 6a). This amount of deviation exceeds the maximum $\delta^{18}O_{Grt}$ variation (0.9‰) induced by temperature changes at 300–650°C. A similar extent of deviation is also observed

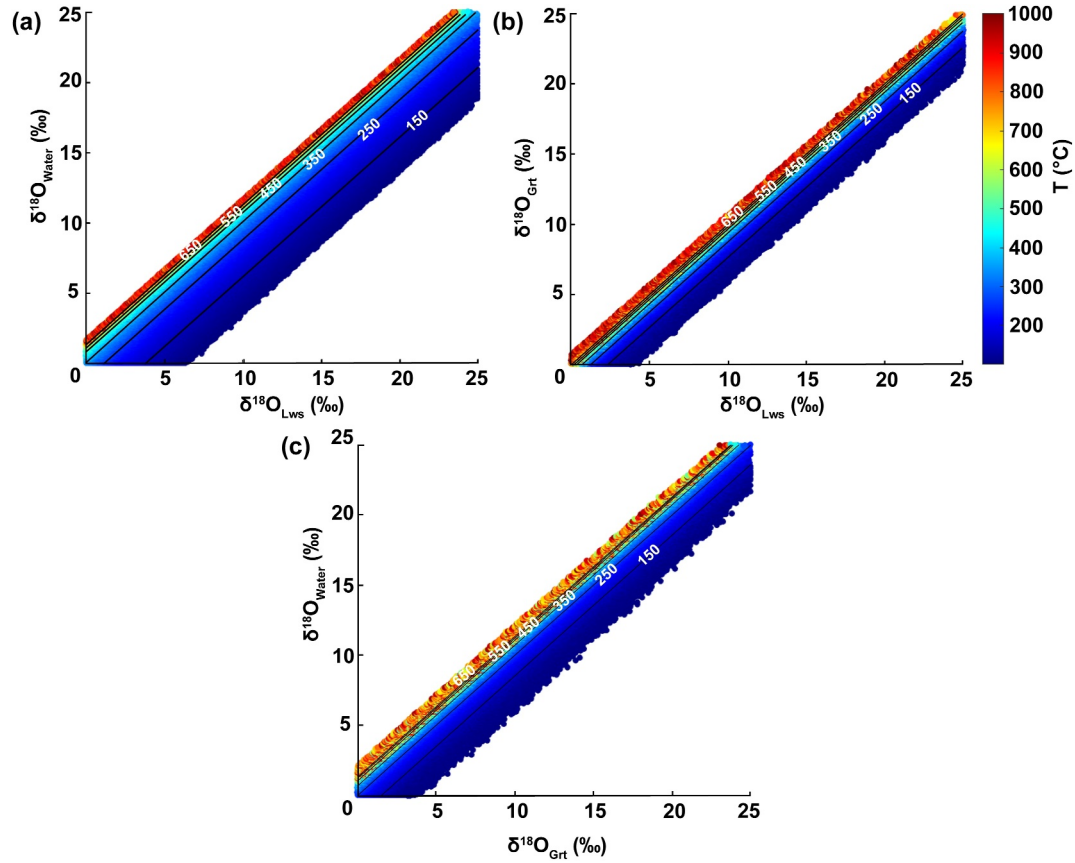

Figure 9. Changes in $\delta^{18}O$ fractionation between $\delta^{18}O_{Lws}$ and $\delta^{18}O_{Water}$ (a), $\delta^{18}O_{Lws}$ and $\delta^{18}O_{Grt}$ (b), and $\delta^{18}O_{Grt}$ and $\delta^{18}O_{Water}$ with varying temperature. The color bar = temperature; Black solid lines = temperature contours.

toward the rims of oscillatory-zoned garnets in the S. Motagua FZ eclogite (MVE04-7-2: up to −2.2‰), the blueschist layer of the Port Macquarie interlayered blueschist/eclogite (17RB-3C: up to 3‰), and the Garnet Ridge xenolith (17GR11: up to −2.1‰) (Figures 6b–6d). All of these deviations suggest that the measured $\delta^{18}O_{Grt}$ variations are not the result of intracrystalline diffusion and/or temperature changes at 300–650°C but instead of isotopic fractionation, such as during fluid-rock interactions. The $\delta^{18}O_{Water}$ corresponding to the $\delta^{18}O_{Grt}$ of the Sivrihisar eclogite garnet and oscillatory-zoned garnet ranges from 7.4 to 14.3‰ based on the calculated extent of $\delta^{18}O$ fractionation at 300–650°C (Table S1 in Supporting Information S2). This $\delta^{18}O_{Water}$ falls within the range of hydrothermally altered upper oceanic crust (7–15‰; e.g., Eiler, 2001) and partially overlaps with that of siliciclastic (meta)sediment (10–20‰; e.g., Eiler, 2001). Therefore, fluids sourced from variable lithologies (altered oceanic crust, (meta)sediment) might have been intermixed in varying proportions and generated $\delta^{18}O_{Water}$ that is different enough to influence $\delta^{18}O_{Grt}$. The intermittent influence of this $\delta^{18}O_{Water}$ might have contributed to abrupt changes in $\delta^{18}O_{Grt}$ toward the garnet rims-to-outermost rims during subduction metamorphism. Inter-mineral $\delta^{18}O$ fractionation is an alternative factor that could have varied $\delta^{18}O_{Grt}$ during subduction metamorphism, but its effect has been interpreted to be negligible (<1‰ variations in $\delta^{18}O_{Grt}$) without external fluid influx (Vho et al., 2020) and the occurrence of quartz and feldspar (Vho et al., 2020; Zheng, 1993), both of which are rare to absent in the analyzed metabasalts.

To evaluate isotopic equilibrium between the analyzed garnet and lawsonite, $\delta^{18}O_{Lws}$ was calculated from the measured $\delta^{18}O_{Grt}$, using the modeled extent of $\delta^{18}O$ fractionation at prograde-to-retrograde conditions (in the range of 300–650°C) (Table S1 in Supporting Information S2) and assuming that both phases were isotopically equilibrated. The calculated $\delta^{18}O_{Lws}$, corresponding to garnet core, rim, and/or outermost rim $\delta^{18}O$, was then compared with measured $\delta^{18}O_{Lws}$. In the Garnet Ridge xenolith and the metabasalts containing oscillatory-zoned garnet, the measured $\delta^{18}O$ of matrix lawsonite overlaps with the calculated $\delta^{18}O_{Lws}$, which corresponds to garnet core-to-rim $\delta^{18}O$ (Figures 6b–6d). This agreement suggests isotopic equilibrium between lawsonite and garnet at

prograde-to-peak conditions. On the other hand, matrix lawsonite in the Sivrihisar eclogite (SV08-283C) has $\delta^{18}O$ corresponding to equilibrium with the garnet core-to-outermost rim $\delta^{18}O$ (Figure 6a), indicating the concurrent growth of lawsonite and garnet at prograde-to-retrograde conditions.

The modeling results of $\delta^{18}O_{Grt}$ diffusion profiles support the widely accepted idea that $\delta^{18}O_{Grt}$ is an excellent recorder of fluid-rock interactions, as it is less affected by intracrystalline diffusion. The significant deviations between the measured $\delta^{18}O_{Grt}$ and the modeled diffusion profiles (>0.9‰) provide compelling evidence supporting fluid-rock interactions during the prograde-to-retrograde metamorphism of the analyzed samples, with fluids originating from various lithologies (e.g., altered oceanic crust, (meta)sediment).

Lawsonite achieved isotopic equilibrium with matrix garnet at various metamorphic stages (prograde-to-retrograde), but many grains reached equilibrium during the growth of garnet core-to-rim, likely under prograde-to-peak conditions (e.g., lawsonite in S. Motagua FZ eclogite, Port Macquarie blueschist, Garnet Ridge eclogite xenolith). This indicates that $\delta^{18}O_{Lws}$ can preserve information about growth conditions rather than undergoing significant modifications through post-crystallization diffusion.

6.4. Lawsonite $\delta^{18}O$: An Indicator of Fluid-Rock Interactions and Protolith $\delta^{18}O$

Around 14% of the analyzed lawsonite grains preserve >1.7‰ intragrain compositional variation (zoning). Such significant $\delta^{18}O_{Lws}$ zoning cannot be attributed to temperature variations at 300–650°C (maximum $\delta^{18}O_{Lws}$ variation: 1.7‰) or to isotopic fractionation by coexisting minerals given the rare occurrence of quartz and the absence of feldspar—two primary phases that fractionate $\delta^{18}O$ ($\Delta\delta^{18}O_{Qz\text{-}Lws}$: 2.5–6.2‰ at 300–650°C; calculated with the parameters from Vho et al. (2019))—especially in the metabasalt and metagabbro samples (Text S1 in Supporting Information S1). Consequently, the most likely contributor to significant $\delta^{18}O$ zoning in metabasite lawsonite is fluid-rock interactions.

Despite occurring in different textural sites (e.g., in veins, matrix), most metabasite lawsonite with >1.7‰ zoning corresponds to heavy $\delta^{18}O_{Fluid}$ (6.2–14.6‰ at 300–650°C; Table S1 in Supporting Information S2). The possible sources of such fluid are siliciclastic-(meta)sediment and/or hydrothermally altered upper oceanic crust (Eiler, 2001). The influence of (meta)sediments on Franciscan metabasalts has been documented by bulk enrichment in large ion lithophile elements (LILE), light rare earth elements (LREE) and/or Th, which are abundant in (meta)sediments (Kang et al., 2022; Sorensen et al., 1997). In addition, the metagreywacke and metapelite-abundant geological settings of the Catalina Schist and New Caledonia Diahot Complex further support the likely interactions with (meta)sediments during the growth of lawsonite (e.g., Fitzherbert et al., 2005; King et al., 2006).

Up to −6‰ zoning can be induced in lawsonite via isotopic fractionation with quartz at 300–650°C. This fractionation effect would be significant in the quartz-abundant garnet-bearing Sivrihisar quartzite (SV08-281D) and effectively demonstrates the substantial $\delta^{18}O_{Lws}$ zoning of individual lawsonite within the quartzite (Figure 4). However, the fractionation effect alone cannot account for the discrepancy between the higher $\delta^{18}O_{Lws}$ calculated from $\delta^{18}O_{Grt}$ at 300–650°C and the measured $\delta^{18}O_{Lws}$ (20.6 ± 1.4 vs. 23.5 ± 1.5‰) (Table S1 in Supporting Information S2), if lawsonite was isotopically equilibrated with quartz and garnet. Therefore, the discrepancy between the calculated and measured $\delta^{18}O_{Lws}$ implies isotopic disequilibrium, in which case garnet formed later than lawsonite and quartz during interactions with heavy-$\delta^{18}O$ fluids (22.4–25‰, calculated from $\delta^{18}O_{Grt}$; Table S1 in Supporting Information S2), potentially sourced from (meta)carbonate sediment (20–35‰; e.g. Eiler, 2001). The later infiltration of (meta)carbonate-sourced fluids is also evident in Sivrihisar blueschist (SV01-75A) as indicated by the high $\delta^{18}O$ of partially retrogressed garnet (Figure 4), which is comparable to (meta)carbonate $\delta^{18}O$ (Eiler, 2001).

The $\delta^{18}O$ of isotopically homogenous lawsonite (<4σ variations) is largely governed by its host rock type, but it varies among subduction complexes. Lawsonite in the Port Macquarie and Franciscan Ring Mt. interlayered blueschist/eclogites (17RB-3C, 17RB-22, LVT-1), S. Motagua FZ eclogite (MVE04-7-2), and Garnet Ridge eclogite xenolith (17GR11) are isotopically lighter than those in the Catalina blueschist (B16-011), Sivrihisar eclogite (SV08-283C) and interlayered blueschist/eclogite (SV01-50A), and Pinchi Lake eclogites (BLR4, 5) (8.8 ± 1.3–10.2 ± 1‰ vs. 11.8 ± 1.2–14.2 ± 0.9‰). However, all of them are significantly heavier than lawsonite in the Corsica metagabbro (C13: 4.0 ± 0.4‰) (Figure 4 and Table 2). If the homogenous $\delta^{18}O_{Lws}$ is the outcome of negligible intracrystalline diffusion, minor isotopic fractionation between coexisting minerals, and the

absence of external fluid influx during lawsonite growth, $\delta^{18}O_{Lws}$ could have inherited protolith $\delta^{18}O$. In this case, the likely mafic protolith is a hydrothermally altered basalt for the metabasalts but an altered gabbro for the Corsica metagabbro (0–6‰; e.g., Eiler, 2001). Despite the similar basaltic protolith, up to a 3–7‰ gap was found between the $\delta^{18}O_{Lws}$ of the Catalina Schist, Sivrihisar Massif, and Pinchi Lake FZ and the other four subduction complexes (Port Macquarie, Franciscan, S. Motagua FZ, Garnet Ridge). This gap might stem from the different contributions of isotopically heavier carbonate (20–35‰) and siliceous sediment (10–20‰) versus lighter mafic-to-ultramafic rock, including serpentinite (0–15‰; e.g., Eiler, 2001), to mafic protolith $\delta^{18}O$. This is supported by the geological settings of the Catalina Schist/USA, Tavşanlı Zone/Sivrihisar Massif, and Pinchi Lake FZ/Canada complex, which are characterized by abundant sedimentary units relative to mafic-to-ultramafic units as compared to the Port Macquarie/Australia, S. Motagua FZ/Guatemala, and Ring Mt./Franciscan (e.g., Davis & Whitney, 2006; Ghent et al., 1996; King et al., 2006; Marroni et al., 2009; Nutman et al., 2013; Och et al., 2003; Tamblyn, Hand, Kelsey, et al., 2020; Tamblyn, Hand, Morrissey, et al., 2020; Wakabayashi, 2015; Whitney et al., 2014). The same reasoning also explains a large $\delta^{18}O_{Lws}$ difference between lawsonite in Sivrihisar metabasalt and metasediment (Figure 4), since sediments likely acted as primary sources of heavy-$\delta^{18}O_{Lws}$ within the metasediment.

Lawsonite in the Rio San Juan metagabbro (IEC15–3.5) is also isotopically homogenous, but its $\delta^{18}O$ (7.9 ± 0.3‰; Figure 4 and Table 2) overlaps with the range of hydrothermally altered basalt, although its likely mafic protolith is inferred to be an altered gabbro given its coarse-grained major matrix phases. This noticeably high $\delta^{18}O_{Lws}$ compared to lawsonite in the Corsica metagabbro (C13) can also result from different contributions of isotopically different lithologies on gabbroic protolith $\delta^{18}O$, as similarly noticed in the metabasalt samples.

In general, lawsonite $\delta^{18}O$ correlates with the protolith $\delta^{18}O$ of lawsonite-bearing host rock as indicated by the lighter $\delta^{18}O_{Lws}$ of metagabbro, the heavier $\delta^{18}O_{Lws}$ of metasediment, and the intermediate $\delta^{18}O_{Lws}$ of metabasalt. Despite sharing a similar mafic protolith (basalt or gabbro), the $\delta^{18}O_{Lws}$ of metabasite shows a considerable range. These $\delta^{18}O_{Lws}$ variations can be attributed to the relative contributions of isotopically different lithologies (lighter mafic-to-ultramafic rocks vs. heavier sediment) to protolith $\delta^{18}O$. Significant intragrain-scale variations (>1.7‰) are recorded in some lawsonite grains, indicating interactions with fluids isotopically different from the protolith or $\delta^{18}O$ fractionation with coexisting minerals (e.g., in metasediment).

6.5. Relationship Between Water-Rock Ratio and Metasomatic Fluid $\delta^{18}O$

Metasomatite is a compositionally hybridized rock that develops by chemical mixing between compositionally distinct lithologies (e.g., mafic and ultramafic rocks, metasediment) during fluid-rock interactions. Since metasomatite is the direct product of fluid-rock interactions, its $\delta^{18}O$ record likely captures the important physical and compositional parameters of metasomatism. The presence of lawsonite in metasomatic rocks indicates that the fluid-rock reaction occurred under HP/LT conditions.

The result of simulations shows that metasomatic fluid predicted from the Tavşanlı metasomatite (TZ10-2.2C) is isotopically heavier (≥13.1‰) than peridotite and its $\delta^{18}O$ converges to 15.1 ± 2.0‰ at $W/R > 1$ but increases drastically at $W/R \leq 1$ (Figure 7). In contrast, two Corsica metasomatites (COR18-PK3, 4) predict metasomatic fluids that are isotopically lighter than calcschist, with $\delta^{18}O_{Water}$ converging to 12.4 ± 2.1–12.7 ± 1.8‰ at $W/R \geq 1$ (Figure 7). In all instances, the simulated probability density tends to increase as the $\delta^{18}O_{Water}$ of each metasomatite approaches its converging value, reaching its maximum at $W/R > 1$ (Figure 7). This result is not surprising, as simulated $\delta^{18}O_{Water}$ will satisfy the following relation (i.e., the limit of Equation 2 as W/R approaches infinity) more often at a wide range of W/R (e.g., $0 \leq W/R \leq 1{,}000$), thereby more converging to a certain value:

$$\lim_{W/R\to\infty} \delta^{18}O_{Water} = \delta^{18}O_{Lws} - 1000\ln\alpha_{Lws-Water} \quad (6)$$

However, it is still noteworthy that W/R at the maximum simulated probability density is consistently predicted to be >1 for all metasomatite cases, even if a much-limited range of W/R ($0 \leq W/R \leq 10$) was used for simulations (Figure S1 in Supporting Information S1).

At $W/R > 1$, the $\delta^{18}O_{Water}$ corresponding to the Tavşanlı metasomatite $\delta^{18}O_{Lws}$ falls within the range of hydrothermally altered basalt and siliciclastic (meta)sediment (Eiler, 2001). Bulk enrichment of Th/La and LILE has

been reported for this metasomatite (Kang et al., 2022), supporting interactions with terrigenous sediments during metasomatism. The Tavşanlı metasomatite could have formed at lower *W/R* (<1) if the fluid had a sufficiently higher $\delta^{18}O$ (>~20‰) than its ultramafic protolith, such as fluid sourced from carbonaceous (meta)sediment (Eiler, 2001). This interpretation is consistent with the high $\delta^{18}O$ of garnet in the Sivrihisar quartzite (SV08-281D) and blueschist (SV01-75A) (Figure 4 and Table 2). The Corsica metasomatites are predicted to have formed at high *W/R* (≥1) through interactions with fluids that were isotopically lighter than their calcschist protoliths (Figure 7). The lower-$\delta^{18}O$ fluids were potentially provided from serpentinite, seawater-altered upper oceanic crust, and siliciclastic (meta)sediment (Eiler, 2001), all of which have been suggested as potential sources that contributed to the bulk Ca, Sr, Cr, and V enrichment of these metasomatites (Vitale Brovarone et al., 2014). Nevertheless, the widespread preservation of disordered carbonaceous material in the regional Corsica metapelitic rocks, unaffected by strong fluid-rock interaction, indicates that this expectation becomes relevant only in the case of major fluid infiltration (e.g., Vitale Brovarone et al., 2020).

Our simulation results further support interpretations of the likely sources of fluids that generated the metasomatites and underscore the importance of high *W/R* (≥1) as a prerequisite for metasomatite formation. However, high *W/R* is not always required to shift precursor rock $\delta^{18}O$ during metasomatism if isotopic exchanges occur between lithologies that are drastically different in $\delta^{18}O$ (e.g., Tavşanlı metasomatite).

7. Conclusions

This study presents an extensive data set of in situ oxygen isotope analyses of lawsonite, a major hydrous mineral in oceanic crust and sediments in subduction zones. Results show that $\delta^{18}O_{Lws}$ largely varies as a function of host rock type, which likely reflects protolith $\delta^{18}O$. However, lawsonite in metabasalt and metagabbro records a wide range of $\delta^{18}O$, reflecting variable contributions from chemically diverse lithologies (carbonaceous and siliceous sediments with higher $\delta^{18}O$ vs. mafic-to-ultramafic rocks with lower $\delta^{18}O$) to protolith $\delta^{18}O$. Significant $\delta^{18}O$ variations also occur in lawsonite (>1.7‰) and garnet (>0.9‰) at the intragrain-scale, suggesting the influence of $\delta^{18}O$ fractionation by coexisting minerals or metasomatic alterations by fluids with different isotopic compositions from the protolith. In structurally coherent subduction terranes, the formation of lawsonite-bearing metasomatite requires either high *W/R* (≥1; e.g., Alpine Corsica/France) or fluids with drastically different $\delta^{18}O$ from the protolith (Tavşanlı/Turkey). In both mélange domains and more structurally coherent terranes in subduction complexes, the $\delta^{18}O$ records of lawsonite and garnet provide evidence of extensive fluid-rock interactions and isotopically diverse sources of metasomatic fluids.

Data Availability Statement

All data for this research are available in Supporting Information S2. The Supporting Information S2 is publicly available on figshare by Kang et al. (2024).

Acknowledgments
We would like to thank Stacia Gordon, Edward Ghent, Sean Mulcahy, George Harlow, and David Hernández-Uribe/Richard Palin for generously providing samples from the Dominican Republic, British Columbia, Franciscan Complex, Guatemala, and Garnet Ridge, respectively. We would also like to acknowledge Chris Harris for his assistance in helping us analyze lawsonite standards. The constructive reviews from the two anonymous reviewers improved this manuscript. This research has been supported by the University of Minnesota Grant-in-Aid program and NSF Grant EAR-1949895 to D.L. Whitney. Additional support was provided in part by the NSF CAREER Grant EAR-2143168 to M. Ibañez-Mejia, and by the European Union's Horizon 2020 research and innovation program (Grant agreement No. 864045) to A. Vitale Brovarone.

References

Anczkiewicz, R., Platt, J. P., Thirlwall, M. F., & Wakabayashi, J. (2004). Franciscan subduction off to a slow start: Evidence from high-precision Lu–Hf garnet ages on high grade-blocks. *Earth and Planetary Science Letters*, *225*(1), 147–161. https://doi.org/10.1016/j.epsl.2004.06.003

Atwater, T. (1970). Implications of plate tectonics for the Cenozoic tectonic evolution of western North America. *GSA Bulletin*, *81*(12), 3513–3536. https://doi.org/10.1130/0016-7606(1970)81[3513:ioptft]2.0.co;2

Baldwin, S. L., Rawling, T., & Fitzgerald, P. G. (2007). Thermochronology of the New Caledonian high-pressure terrane: Implications for middle Tertiary plate boundary processes in the southwest Pacific. In *Convergent margin terranes and associated regions: A tribute to W.G. Ernst* (Vol. 419, pp. 117–134). Geological Society of America.

Bebout, G. E., & Barton, M. D. (1993). Metasomatism during subduction: Products and possible paths in the Catalina Schist, California. *Chemical Geology*, *108*(1), 61–92. https://doi.org/10.1016/0009-2541(93)90318-d

Bebout, G. E., & Barton, M. D. (2002). Tectonic and metasomatic mixing in a high-T, subduction-zone mélange—Insights into the geochemical evolution of the slab–mantle interface. *Chemical Geology*, *187*(1), 79–106. https://doi.org/10.1016/s0009-2541(02)00019-0

Bovay, T., Rubatto, D., & Lanari, P. (2021). Pervasive fluid-rock interaction in subducted oceanic crust revealed by oxygen isotope zoning in garnet. *Contributions to Mineralogy and Petrology*, *176*(7), 55. https://doi.org/10.1007/s00410-021-01806-4

Brown, E. H., & Ghent, E. D. (1983). Mineralogy and phase relations in the blueschist facies of the Black Butte and Ball Rock areas, northern California Coast Ranges. *American Mineralogist*, *68*(3–4), 365–372.

Brueckner, H. K., Avé Lallemant, H. G., Sisson, V. B., Harlow, G. E., Hemming, S. R., Martens, U., et al. (2009). Metamorphic reworking of a high pressure–low temperature mélange along the Motagua fault, Guatemala: A record of Neocomian and Maastrichtian transpressional tectonics. *Earth and Planetary Science Letters*, *284*(1), 228–235. https://doi.org/10.1016/j.epsl.2009.04.032

Clarke, G. L., Aitchison, J. C., & Cluzel, D. (1997). Eclogites and blueschists of the Pam Peninsula, NE New Caledonia: A reappraisal. *Journal of Petrology*, *38*(7), 843–876. https://doi.org/10.1093/petrology/38.7.843

Cluzel, D., Adams, C. J., Meffre, S., Campbell, H., & Maurizot, P. (2010). Discovery of Early Cretaceous rocks in New Caledonia: New geochemical and U-Pb zircon age constraints on the transition from subduction to marginal breakup in the southwest Pacific. *The Journal of Geology*, *118*(4), 381–397. https://doi.org/10.1086/652779

Coghlan, R. A. N. (1990). Studies in diffusional transport: Grain boundary transport of oxygen in feldspars, diffusion of oxygen, strontium and the REEs in garnet, and thermal histories of granitic intrusions in south-central Maine using oxygen isotopes. (Doctoral dissertation). Brown University. Retrieved from https://www.proquest.com/docview/303802606

Collins, N. C., Bebout, G. E., Angiboust, S., Agard, P., Scambelluri, M., Crispini, L., & John, T. (2015). Subduction zone metamorphic pathway for deep carbon cycling: II. Evidence from HP/UHP metabasaltic rocks and ophicarbonates. *Chemical Geology*, *412*, 132–150. https://doi.org/10.1016/j.chemgeo.2015.06.012

Crank, J. (1979). *The mathematics of diffusion*. Clarendon Press.

Cruz-Uribe, A. M., Page, F. Z., Lozier, E., Feineman, M. D., Zack, T., Mertz-Kraus, R., et al. (2021). Trace element and isotopic zoning of garnetite veins in amphibolitized eclogite, Franciscan Complex, California, USA. *Contributions to Mineralogy and Petrology*, *176*(5), 41. https://doi.org/10.1007/s00410-021-01795-4

Davis, P. B., & Whitney, D. L. (2006). Petrogenesis of lawsonite and epidote eclogite and blueschist, Sivrihisar Massif, Turkey. *Journal of Metamorphic Geology*, *24*(9), 823–849. https://doi.org/10.1111/j.1525-1314.2006.00671.x

Davis, P. B., & Whitney, D. L. (2008). Petrogenesis and structural petrology of high-pressure metabasalt pods, Sivrihisar, Turkey. *Contributions to Mineralogy and Petrology*, *156*(2), 217–241. https://doi.org/10.1007/s00410-008-0282-4

Dickinson, W. R. (1997). Overview: Tectonic implications of Cenozoic volcanism in coastal California. *GSA Bulletin*, *109*(8), 936–954. https://doi.org/10.1130/0016-7606(1997)109<0936:otiocv>2.3.co;2

Eiler, J. M. (2001). Oxygen isotope variations of basaltic lavas and upper mantle rocks. *Reviews in Mineralogy and Geochemistry*, *43*(1), 319–364. https://doi.org/10.2138/gsrmg.43.1.319

Eiler, J. M., Graham, C., & Valley, J. W. (1997). SIMS analysis of oxygen isotopes: Matrix effects in complex minerals and glasses. *Chemical Geology*, *138*(3), 221–244. https://doi.org/10.1016/s0009-2541(97)00015-6

Elliott, T. (2004). Tracers of the slab. In *Inside the subduction factory* (Vol. 138, pp. 23–45). American Geophysical Union.

Endo, S., Wallis, S. R., Tsuboi, M., Torres de León, R., & Solari, L. A. (2012). Metamorphic evolution of lawsonite eclogites from the southern Motagua fault zone, Guatemala: Insights from phase equilibria and Raman spectroscopy. *Journal of Metamorphic Geology*, *30*(2), 143–164. https://doi.org/10.1111/j.1525-1314.2011.00960.x

Ernst, W. G. (1993). Metamorphism of Franciscan tectonostratigraphic assemblage, Pacheco Pass area, east-central Diablo Range, California coast ranges. *GSA Bulletin*, *105*(5), 618–636. https://doi.org/10.1130/0016-7606(1993)105<0618:moftap>2.3.co;2

Ernst, W. G., & Liu, J. (1998). Experimental phase-equilibrium study of Al- and Ti-contents of calcic amphibole in MORB; a semiquantitative thermobarometer. *American Mineralogist*, *83*(9–10), 952–969. https://doi.org/10.2138/am-1998-9-1004

Ernst, W. G., & McLaughlin, R. J. (2012). Mineral parageneses, regional architecture, and tectonic evolution of Franciscan metagraywackes, Cape Mendocino-Garberville-Covelo 30′×60′ quadrangles, northwest California. *Tectonics*, *31*(1), TC1001. https://doi.org/10.1029/2011tc002987

Errico, J. C., Barnes, J. D., Strickland, A., & Valley, J. W. (2013). Oxygen isotope zoning in garnets from Franciscan eclogite blocks: Evidence for rock–buffered fluid interaction in the mantle wedge. *Contributions to Mineralogy and Petrology*, *166*(4), 1161–1176. https://doi.org/10.1007/s00410-013-0915-0

Fitzherbert, J. A., Clarke, G. L., & Powell, R. (2005). Preferential retrogression of high-P metasediments and the preservation of blueschist to eclogite facies metabasite during exhumation, Diahot terrane, NE New Caledonia. *Lithos*, *83*(1), 67–96. https://doi.org/10.1016/j.lithos.2005.01.005

Fornash, K. F., Cosca, M. A., & Whitney, D. L. (2016). Tracking the timing of subduction and exhumation using $^{40}Ar/^{39}Ar$ phengite ages in blueschist- and eclogite-facies rocks (Sivrihisar, Turkey). *Contributions to Mineralogy and Petrology*, *171*(7), 67. https://doi.org/10.1007/s00410-016-1268-2

Fornash, K. F., & Whitney, D. L. (2020). Lawsonite-rich layers as records of fluid and element mobility in subducted crust (Sivrihisar Massif, Turkey). *Chemical Geology*, *533*, 119356. https://doi.org/10.1016/j.chemgeo.2019.119356

Fornash, K. F., Whitney, D. L., & Seaton, N. C. A. (2019). Lawsonite composition and zoning as an archive of metamorphic processes in subduction zones. *Geosphere*, *15*(1), 24–46. https://doi.org/10.1130/ges01455.1

Forneris, J. F., & Holloway, J. R. (2003). Phase equilibria in subducting basaltic crust: Implications for H_2O release from the slab. *Earth and Planetary Science Letters*, *214*(1), 187–201. https://doi.org/10.1016/s0012-821x(03)00305-4

Fukui, S., Watanabe, T., Itaya, T., & Leitch, E. C. (1995). Middle Ordovician high PT metamorphic rocks in eastern Australia: Evidence from K-Ar ages. *Tectonics*, *14*(4), 1014–1020. https://doi.org/10.1029/94tc01317

Gauthiez Putallaz, L. (2017). Tracing fluids during medium to ultra-high pressure metamorphism: Insights by combined in situ oxygen isotopes and trace element analysis. (Doctoral dissertation). The Australian National University. https://doi.org/10.25911/5C8236FB1D0D3

Ghent, E., Tinkham, D., & Marr, R. (2009). Lawsonite eclogites from the Pinchi Lake area, British Columbia—New P–T estimates and interpretation. *Lithos*, *109*(3), 248–253. https://doi.org/10.1016/j.lithos.2008.06.018

Ghent, E. D., Erdmer, P., Archibald, D. A., & Stout, M. Z. (1996). Pressure—Temperature and tectonic evolution of Triassic lawsonite—Aragonite blueschists from Pinchi Lake, British Columbia. *Canadian Journal of Earth Sciences*, *33*(5), 800–810. https://doi.org/10.1139/e96-061

Ghent, E. D., Stout, M. Z., & Erdmer, P. (1993). Pressure-temperature evolution of lawsonite-bearing eclogites, Pinchi Lake, British Columbia. *Journal of Metamorphic Geology*, *11*(2), 279–290. https://doi.org/10.1111/j.1525-1314.1993.tb00147.x

Grove, M., & Bebout, G. E. (1995). Cretaceous tectonic evolution of coastal southern California: Insights from the Catalina Schist. *Tectonics*, *14*(6), 1290–1308. https://doi.org/10.1029/95tc01931

Grove, M., Bebout, G. E., Jacobson, C. E., Barth, A. P., Kimbrough, D. L., King, R. L., et al. (2008). The Catalina Schist: Evidence for middle Cretaceous subduction erosion of southwestern North America. In *Formation and applications of the sedimentary record in arc collision zones* (Vol. 436, pp. 335–361). Geological Society of America.

Grove, T. L., Chatterjee, N., Parman, S. W., & Médard, E. (2006). The influence of H_2O on mantle wedge melting. *Earth and Planetary Science Letters*, *249*(1), 74–89. https://doi.org/10.1016/j.epsl.2006.06.043

Harlow, G. E., Hemming, S. R., Avé Lallemant, H. G., Sisson, V. B., & Sorensen, S. S. (2004). Two high-pressure–low-temperature serpentinite-matrix mélange belts, Motagua fault zone, Guatemala: A record of Aptian and Maastrichtian collisions. *Geology*, *32*(1), 17–20. https://doi.org/10.1130/g19990.1

Harvey, K. M., Walker, S., Starr, P. G., Penniston-Dorland, S. C., Kohn, M. J., & Baxter, E. F. (2021). A mélange of subduction ages: Constraints on the timescale of shear zone development and underplating at the subduction interface, Catalina schist (CA, USA). *Geochemistry, Geophysics, Geosystems*, *22*(9), e2021GC009790. https://doi.org/10.1029/2021gc009790

Hernández-Uribe, D., & Palin, R. M. (2019). Catastrophic shear-removal of subcontinental lithospheric mantle beneath the Colorado Plateau by the subducted Farallon slab. *Scientific Reports*, *9*(1), 8153. https://doi.org/10.1038/s41598-019-44628-y

Kang, P., Fornash, K. F., & Whitney, D. L. (2020). Controls on development of different mineral assemblages in gabbro and basalt during subduction metamorphism. *Contributions to Mineralogy and Petrology*, *175*(113), 113. https://doi.org/10.1007/s00410-020-01753-6

Kang, P., Martin, L., Vitale Brovarone, A., & Whitney, D. L. (2024). Supporting information S2.xlsx (version 1) [Dataset]. *Figshare*. https://doi.org/10.6084/m9.figshare.25389388.v1

Kang, P., Whitney, D. L., Martin, L. A. J., & Fornash, K. F. (2022). Trace and rare Earth element compositions of lawsonite as a chemical tracer of metamorphic processes in subduction zones. *Journal of Petrology*, *63*(8), egac065. https://doi.org/10.1093/petrology/egac065

Kelley, K. A., Plank, T., Newman, S., Stolper, E. M., Grove, T. L., Parman, S., & Hauri, E. H. (2010). Mantle melting as a function of water content beneath the Mariana Arc. *Journal of Petrology*, *51*(8), 1711–1738. https://doi.org/10.1093/petrology/egq036

King, R. L., Bebout, G. E., Moriguti, T., & Nakamura, E. (2006). Elemental mixing systematics and Sr–Nd isotope geochemistry of mélange formation: Obstacles to identification of fluid sources to arc volcanics. *Earth and Planetary Science Letters*, *246*(3), 288–304. https://doi.org/10.1016/j.epsl.2006.03.053

Kohn, M. J. (1993). Modeling of prograde mineral $\delta^{18}O$ changes in metamorphic systems. *Contributions to Mineralogy and Petrology*, *113*(2), 249–261. https://doi.org/10.1007/bf00283232

Kohn, M. J., & Valley, J. W. (1998). Obtaining equilibrium oxygen isotope fractionations from rocks: Theory and examples. *Contributions to Mineralogy and Petrology*, *132*(3), 209–224. https://doi.org/10.1007/s004100050418

Krebs, M., Maresch, W. V., Schertl, H., Münker, C., Baumann, A., Draper, G., et al. (2008). The dynamics of intra-oceanic subduction zones: A direct comparison between fossil petrological evidence (Rio San Juan Complex, Dominican Republic) and numerical simulation. *Lithos*, *103*(1–2), 106–137. https://doi.org/10.1016/j.lithos.2007.09.003

Krebs, M., Schertl, H. P., Maresch, W. V., & Draper, G. (2011). Mass flow in serpentinite-hosted subduction channels: P–T–t path patterns of metamorphic blocks in the Rio San Juan mélange (Dominican Republic). *Journal of Asian Earth Sciences*, *42*(4), 569–595. https://doi.org/10.1016/j.jseaes.2011.01.011

Krogh, E. J., Oh, C. W., & Liou, J. C. (1994). Polyphase and anticlockwise P-T evolution for Franciscan eclogites and blueschists from Jenner, California, USA. *Journal of Metamorphic Geology*, *12*(2), 121–134. https://doi.org/10.1111/j.1525-1314.1994.tb00008.x

Marroni, M., Pandolfi, L., Principi, G., Malasoma, A., & Meneghini, F. (2009). Deformation history of the eclogite- and jadeitite-bearing mélange from North Motagua fault zone, Guatemala: Insights in the processes of a fossil subduction channel. *Geological Journal*, *44*(2), 167–190. https://doi.org/10.1002/gj.1145

Martin, L. A. J., Hermann, J., Gauthiez-Putallaz, L., Whitney, D. L., Vitale Brovarone, A., Fornash, K. F., & Evans, N. J. (2014). Lawsonite geochemistry and stability—Implication for trace element and water cycles in subduction zones. *Journal of Metamorphic Geology*, *32*(5), 455–478. https://doi.org/10.1111/jmg.12093

Martin, L. A. J., Rubatto, D., Crépisson, C., Hermann, J., Putlitz, B., & Vitale-Brovarone, A. (2014). Garnet oxygen analysis by SHRIMP-SI: Matrix corrections and application to high-pressure metasomatic rocks from Alpine Corsica. *Chemical Geology*, *374–375*, 25–36. https://doi.org/10.1016/j.chemgeo.2014.02.010

Martin, L. A. J., Rubatto, D., Vitale Brovarone, A., & Hermann, J. (2011). Late Eocene lawsonite-eclogite facies metasomatism of a granulite sliver associated to ophiolites in Alpine Corsica. *Lithos*, *125*(1), 620–640. https://doi.org/10.1016/j.lithos.2011.03.015

Melnik, A. E., Li, Q. L., Li, J., Tang, G. Q., Feng, L. J., Li, J. H., et al. (2023). LM-19 lawsonite: A potential reference material for in situ oxygen isotope determination in lawsonite by ion microprobe. *Journal of Analytical Atomic Spectrometry*, *38*(1), 221–228. https://doi.org/10.1039/d2ja00301e

Mulcahy, S. R., King, R. L., & Vervoort, J. D. (2009). Lawsonite Lu-Hf geochronology: A new geochronometer for subduction zone processes. *Geology*, *37*(11), 987–990. https://doi.org/10.1130/g30292a.1

Mulcahy, S. R., Vervoort, J. D., & Renne, P. R. (2014). Dating subduction-zone metamorphism with combined garnet and lawsonite Lu-Hf geochronology. *Journal of Metamorphic Geology*, *32*(5), 515–533. https://doi.org/10.1111/jmg.12092

Nutman, A. P., Buckman, S., Hidaka, H., Kamiichi, T., Belousova, E., & Aitchison, J. (2013). Middle Carboniferous-Early Triassic eclogite-blueschist blocks within a serpentinite mélange at Port Macquarie, eastern Australia: Implications for the evolution of Gondwana's eastern margin. *Gondwana Research*, *24*(3–4), 1038–1050. https://doi.org/10.1016/j.gr.2013.01.009

Och, D. J., Leitch, E. C., Caprarelli, G., & Watanabe, T. (2003). Blueschist and eclogite in tectonic melange, Port Macquarie, New South Wales, Australia. *Mineralogical Magazine*, *67*(4), 609–624. https://doi.org/10.1180/0026461036740121

Okay, A. I. (1980). Mineralogy, petrology, and phase relations of glaucophane-lawsonite zone blueschists from the Tavşanlı Region, Northwest Turkey. *Contributions to Mineralogy and Petrology*, *72*(3), 243–255. https://doi.org/10.1007/bf00376143

Okay, A. I. (1982). Incipient blueschist metamorphism and metasomatism in the Tavşanlı region, Northwest Turkey. *Contributions to Mineralogy and Petrology*, *79*(4), 361–367. https://doi.org/10.1007/bf01132065

Okay, A. I. (1986). High-pressure/low-temperature metamorphic rocks of Turkey. *Geological Society of America Memoir*, *164*, 333–347. https://doi.org/10.1130/mem164-p333

Page, F. Z., Armstrong, L. S., Essene, E. J., & Mukasa, S. B. (2007). Prograde and retrograde history of the Junction School eclogite, California, and an evaluation of garnet-phengite-clinopyroxene thermobarometry. *Contributions to Mineralogy and Petrology*, *153*(5), 533–555. https://doi.org/10.1007/s00410-006-0161-9

Page, F. Z., Essene, E. J., Mukasa, S. B., & Valley, J. W. (2014). A garnet–zircon oxygen isotope record of subduction and exhumation fluids from the Franciscan Complex, California. *Journal of Petrology*, *55*(1), 103–131. https://doi.org/10.1093/petrology/egt062

Page, F. Z., Kita, N. T., & Valley, J. W. (2010). Ion microprobe analysis of oxygen isotopes in garnets of complex chemistry. *Chemical Geology*, *270*(1), 9–19. https://doi.org/10.1016/j.chemgeo.2009.11.001

Paterson, I. A., & Harakal, J. E. (1974). Potassium–argon dating of blueschists from Pinchi Lake, central British Columbia. *Canadian Journal of Earth Sciences*, *11*(7), 1007–1011. https://doi.org/10.1139/e74-097

Penniston-Dorland, S. C., & Harvey, K. M. (2023). Constraints on tectonic processes in subduction mélange: A review of insights from the Catalina Schist (CA, USA). *Geosystems and Geoenvironment*, *2*(3), 100190. https://doi.org/10.1016/j.geogeo.2023.100190

Penniston-Dorland, S. C., Sorensen, S. S., Ash, R. D., & Khadke, S. V. (2010). Lithium isotopes as a tracer of fluids in a subduction zone mélange: Franciscan Complex, CA. *Earth and Planetary Science Letters*, *292*(1), 181–190. https://doi.org/10.1016/j.epsl.2010.01.034

Piccoli, F., Vitale Brovarone, A., & Ague, J. J. (2018). Field and petrological study of metasomatism and high-pressure carbonation from lawsonite eclogite-facies terrains, Alpine Corsica. *Lithos*, *304–307*, 16–37. https://doi.org/10.1016/j.lithos.2018.01.026

Plunder, A., Agard, P., Chopin, C., Pourteau, A., & Okay, A. I. (2015). Accretion, underplating and exhumation along a subduction interface: From subduction initiation to continental subduction (Tavşanlı zone, W. Turkey). *Lithos*, *226*, 233–254. https://doi.org/10.1016/j.lithos.2015.01.007

Pourteau, A., Scherer, E. E., Schorn, S., Bast, R., Schmidt, A., & Ebert, L. (2019). Thermal evolution of an ancient subduction interface revealed by Lu–Hf garnet geochronology, Halilbağı Complex (Anatolia). *Geoscience Frontiers*, *10*(1), 127–148. https://doi.org/10.1016/j.gsf.2018.03.004

Ratschbacher, L., Franz, L., Min, M., Bachmann, R., Martens, U., Stanek, K., et al. (2009). The North American-Caribbean plate boundary in Mexico-Guatemala-Honduras. In *The geology and evolution of the region between North and South America* (Vol. 328, pp. 219–293). Geological Society, London, Special Publications.

Ravna, E. J. K., Andersen, T. B., Jolivet, L., & de Capitani, C. (2010). Cold subduction and the formation of lawsonite eclogite—Constraints from prograde evolution of eclogitized pillow lava from Corsica. *Journal of Metamorphic Geology*, *28*(4), 381–395. https://doi.org/10.1111/j.1525-1314.2010.00870.x

Rawling, T. J., & Lister, G. S. (2002). Large-scale structure of the eclogite–blueschist belt of New Caledonia. *Journal of Structural Geology*, *24*(8), 1239–1258. https://doi.org/10.1016/s0191-8141(01)00128-6

Schmidt, M. W., & Poli, S. (1998). Experimentally based water budgets for dehydrating slabs and consequences for arc magma generation. *Earth and Planetary Science Letters*, *163*(1), 361–379. https://doi.org/10.1016/s0012-821x(98)00142-3

Scicchitano, M. R., Jollands, M. C., Williams, I. S., Hermann, J., Rubatto, D., Kita, N. T., et al. (2022). Oxygen diffusion in garnet: Experimental calibration and implications for timescales of metamorphic processes and retention of primary O isotopic signatures. *American Mineralogist*, *107*(7), 1425–1441. https://doi.org/10.2138/am-2022-7970

Sharp, Z. (2007). *Principles of stable isotope geochemistry*. Pearson/Prentice Hall.

Smith, D., Connelly, J. N., Manser, K., Moser, D. E., Housh, T. B., McDowell, F. W., & Mack, L. E. (2004). Evolution of Navajo eclogites and hydration of the mantle wedge below the Colorado Plateau, southwestern United States. *Geochemistry, Geophysics, Geosystems*, *5*(4), Q04005. https://doi.org/10.1029/2003gc000675

Sorensen, S. S., Grossman, J. N., & Perfit, M. R. (1997). Phengite-hosted LILE enrichment in eclogite and related rocks: Implications for fluid-mediated mass transfer in subduction zones and arc magma genesis. *Journal of Petrology*, *38*(1), 3–34. https://doi.org/10.1093/petrology/38.1.3

Spandler, C., Pettke, T., & Rubatto, D. (2011). Internal and external fluid sources for eclogite-facies veins in the Monviso meta-ophiolite, Western Alps: Implications for fluid flow in subduction zones. *Journal of Petrology*, *52*(6), 1207–1236. https://doi.org/10.1093/petrology/egr025

Tamblyn, R., Hand, M., Kelsey, D., Anczkiewicz, R., & Och, D. (2020). Subduction and accumulation of lawsonite eclogite and garnet blueschist in eastern Australia. *Journal of Metamorphic Geology*, *38*(2), 157–182. https://doi.org/10.1111/jmg.12516

Tamblyn, R., Hand, M., Morrissey, L., Zack, T., Phillips, G., & Och, D. (2020). Resubduction of lawsonite eclogite within a serpentinite-filled subduction channel. *Contributions to Mineralogy and Petrology*, *175*(8), 74. https://doi.org/10.1007/s00410-020-01712-1

Taylor, H. P., & Coleman, R. G. (1968). O^{18}/O^{16} ratios of coexisting minerals in glaucophane-bearing metamorphic rocks. *GSA Bulletin*, *79*(12), 1727–1756. https://doi.org/10.1130/0016-7606(1968)79[1727:orocmi]2.0.co;2

Thomas, Z., Rivers, T., Brumm, R., & Kronz, A. (2004). Cold subduction of oceanic crust Implications from a lawsonite eclogite from the Dominican Republic. *European Journal of Mineralogy*, *16*(6), 909–916. https://doi.org/10.1127/0935-1221/2004/0016-0909

Tsujimori, T., Matsumoto, K., Wakabayashi, J., & Liou, J. G. (2006). Franciscan eclogite revisited: Reevaluation of the P–T evolution of tectonic blocks from Tiburon Peninsula, California, U.S.A. *Mineralogy and Petrology*, *88*(1–2), 243–267. https://doi.org/10.1007/s00710-006-0157-1

Tsujimori, T., Sisson, V. B., Liou, J. G., Harlow, G. E., & Sorensen, S. S. (2006). Petrologic characterization of Guatemalan lawsonite eclogite: Eclogitization of subducted oceanic crust in a cold subduction zone. In *Ultrahigh-pressure metamorphism: Deep continental subduction* (Vol. 403, pp. 147–168). Geological Society of America.

Usui, T., Nakamura, E., & Helmstaedt, H. (2006). Petrology and geochemistry of eclogite xenoliths from the Colorado Plateau: Implications for the evolution of subducted oceanic crust. *Journal of Petrology*, *47*(5), 929–964. https://doi.org/10.1093/petrology/egi101

Usui, T., Nakamura, E., Kobayashi, K., Maruyama, S., & Helmstaedt, H. (2003). Fate of the subducted Farallon plate inferred from eclogite xenoliths in the Colorado Plateau. *Geology*, *31*(7), 589–592. https://doi.org/10.1130/0091-7613(2003)031<0589:fotsfp>2.0.co;2

Valley, J. W., Kitchen, N., Kohn, M. J., Niendorf, C. R., & Spicuzza, M. J. (1995). UWG-2, a garnet standard for oxygen isotope ratios: Strategies for high precision and accuracy with laser heating. *Geochimica et Cosmochimica Acta*, *59*(24), 5223–5231. https://doi.org/10.1016/0016-7037(95)00386-x

Vho, A., Lanari, P., & Rubatto, D. (2019). An internally-consistent database for oxygen isotope fractionation between minerals. *Journal of Petrology*, *60*(11), 2101–2129. https://doi.org/10.1093/petrology/egaa001

Vho, A., Lanari, P., Rubatto, D., & Hermann, J. (2020). Tracing fluid transfers in subduction zones: An integrated thermodynamic and $\delta^{18}O$ fractionation modelling approach. *Solid Earth*, *11*(2), 307–328. https://doi.org/10.5194/se-11-307-2020

Vielzeuf, D., Champenois, M., Valley, J. W., Brunet, F., & Devidal, J. L. (2005). SIMS analyses of oxygen isotopes: Matrix effects in Fe–Mg–Ca garnets. *Chemical Geology*, *223*(4), 208–226. https://doi.org/10.1016/j.chemgeo.2005.07.008

Vitale Brovarone, A. (2013). Lawsonite-bearing omphacitites from Alpine Corsica (France). *International Journal of Earth Sciences*, *102*(5), 1377–1379. https://doi.org/10.1007/s00531-013-0901-9

Vitale Brovarone, A., & Agard, P. (2013). True metamorphic isograds or tectonically sliced metamorphic sequence? New high-spatial resolution petrological data for the New Caledonia case study. *Contributions to Mineralogy and Petrology*, *166*(2), 451–469. https://doi.org/10.1007/s00410-013-0885-2

Vitale Brovarone, A., Agard, P., Monié, P., Chauvet, A., & Rabaute, A. (2018). Tectonic and metamorphic architecture of the HP belt of New Caledonia. *Earth-Science Reviews*, *178*, 48–67. https://doi.org/10.1016/j.earscirev.2018.01.006

Vitale Brovarone, A., Alard, O., Beyssac, O., Martin, L., & Picatto, M. (2014). Lawsonite metasomatism and trace element recycling in subduction zones. *Journal of Metamorphic Geology*, *32*(5), 489–514. https://doi.org/10.1111/jmg.12074

Vitale Brovarone, A., Groppo, C., Hetényi, G., Compagnoni, R., & Malavieille, J. (2011). Coexistence of lawsonite-bearing eclogite and blueschist: Phase equilibria modelling of Alpine Corsica metabasalts and petrological evolution of subducting slabs. *Journal of Metamorphic Geology*, *29*(5), 583–600. https://doi.org/10.1111/j.1525-1314.2011.00931.x

Vitale Brovarone, A., & Herwartz, D. (2013). Timing of HP metamorphism in the Schistes Lustrés of Alpine Corsica: New Lu–Hf garnet and lawsonite ages. *Lithos*, *172–173*, 175–191. https://doi.org/10.1016/j.lithos.2013.03.009

Vitale Brovarone, A., Tumiati, S., Piccoli, F., Ague, J. J., Connolly, J. A. D., & Beyssac, O. (2020). Fluid-mediated selective dissolution of subducting carbonaceous material: Implications for carbon recycling and fluid fluxes at forearc depths. *Chemical Geology*, *549*, 119682. https://doi.org/10.1016/j.chemgeo.2020.119682

Wakabayashi, J. (2015). Anatomy of a subduction complex: Architecture of the Franciscan Complex, California, at multiple length and time scales. *International Geology Review*, *57*(5–8), 669–746. https://doi.org/10.1080/00206814.2014.998728

Whitney, D. L., & Evans, B. W. (2010). Abbreviations for names of rock-forming minerals. *American Mineralogist*, *95*(1), 185–187. https://doi.org/10.2138/am.2010.3371

Whitney, D. L., Fornash, K. F., Kang, P., Ghent, E. D., Martin, L., Okay, A. I., & Vitale Brovarone, A. (2020). Lawsonite composition and zoning as tracers of subduction processes: A global review. *Lithos*, *370–371*, 105636. https://doi.org/10.1016/j.lithos.2020.105636

Whitney, D. L., Teyssier, C., Seaton, N. C. A., & Fornash, K. F. (2014). Petrofabrics of high-pressure rocks exhumed at the slab-mantle interface from the "point of no return" in a subduction zone (Sivrihisar, Turkey). *Tectonics*, *33*(12), 2315–2341. https://doi.org/10.1002/2014tc003677

You, C. F., Castillo, P. R., Gieskes, J. M., Chan, L. H., & Spivack, A. J. (1996). Trace element behavior in hydrothermal experiments: Implications for fluid processes at shallow depths in subduction zones. *Earth and Planetary Science Letters*, *140*(1), 41–52. https://doi.org/10.1016/0012-821x(96)00049-0

Zheng, Y. F. (1993). Calculation of oxygen isotope fractionation in anhydrous silicate minerals. *Geochimica et Cosmochimica Acta*, *57*(5), 1079–1091. https://doi.org/10.1016/0016-7037(93)90042-u